AMPHIPHILE SELF-ASSEMBLY AND PHASE EVOLUTION IN REACTIVE ENVIRONMENTS

BY

DEBORAH YANG HAO LIU

DISSERTATION

Submitted in partial fulfillment of the requirements
for the degree of Doctor of Philosophy in Materials Science and Engineering
in the Graduate College of the
University of Illinois Urbana-Champaign, 2022

Urbana, Illinois

Doctoral Committee:

Associate Professor Christopher Evans, Chair
Research Assistant Professor Daniel V. Krogstad
Associate Professor Cecilia Leal
Professor Paul Braun

ABSTRACT

In this work, we present two different systems of self-assembled amphiphile phase evolution under elevated temperatures. Characterization is largely performed with small-angle x-ray scattering. In the first system, a ternary mixture of block copolymer, epoxy resin, and ionic liquid is found to exhibit a wide variety of lyotropic phases typical to block copolymer self-assembly. The ionic liquid is found to modify the phase behavior of the block copolymer-epoxy mixture in a manner similar to selective solvent phase modification of block copolymers. The phase transitions exhibited in the ternary phase diagram can largely be understood through considerations of polymer volume and chain swelling. The system was then subjected to an elevated temperature such that the epoxy resin cured, and transformed from an unpolymerized liquid resin to a high molecular weight epoxy matrix. Phase transitions were observed at nearly every composition. In one case, an in-situ curing reaction wherein SAXS was performed continuously throughout the curing cycle revealed nearly continuous order-order transitions throughout the curing cycle. The variety of phase transitions observed suggests significant future opportunities in engineering materials with a wide variety of possible nanostructures.

In the second system, a mixture of acylglycerols and long-chain alkyl oils was subjected to thermal breakdown in the presence of metal in autoclave experiments. This work was motivated by a gap in the understanding of how acylglycerols, which are materials of significant economic importance, cause the corrosion of metals. Systematic corrosion experiments were performed. Acylglycerols were found to break down readily in autoclave conditions, releasing significant amounts of decomposition products early in the process. These experiments informed follow-on experiments, which sought to design reverse micelle-forming solutions comprised of

molecules found in acylglycerol thermal breakdown. By exploiting the amphiphilic nature of monoglycerides, we demonstrate that reverse micelles can incorporate both fatty acid and water into their structures. This work serves as preliminary experiments for the design of biofeedstock mixtures that neutralize corrosive species by sequestering the more corrosive (i.e. more polar) species.

ACKNOWLEDGMENTS

This work is the result of a great deal of assistance from many individuals. The feedback and advice from my committee members was especially valuable. I would like to particularly thank my research director, Dan Krogstad, for his extensive help throughout my PhD (as well as his patience and support when life sometimes got in the way of research). Special thanks also to Chris Evans and the members of the Evans group who have been my graduate student 'tribe' over the years.

This work was carried out in part in the Materials Research Laboratory Central Research Facilities, University of Illinois, and I gratefully acknowledge the members of staff who provided valuable experimental assistance. Thanks to Dr. Roddel Remy, Dr. Mauro Sardela, Dr. James Lee, Dr. Juan Rodriguez, Lou Ann Miller, and Dr. Kathy Walsh for assistance with various techniques. This research also used resources of the Advanced Photon Source at Argonne National Laboratory. Thank you to Dr. Soenke Seifert and Dr. Sungsik Lee at Argonne for their assistance in performing x-ray scattering experiments.

I would like to thank the many graduate students and postdocs I worked with over the years, and for the generous help freely offered by many when I needed advice or another brain to look at my data. Thanks also to the various undergrads who have assisted on my projects for your enthusiasm and hard work.

Portions of this work were funded through a YIP award funded by the AFOSR Low Density Materials program under grant number FA9550-17-1-0128. Additional technical and financial support from BP through the BP International Centre for Advanced Materials (BP-ICAM).

For my family

TABLE OF CONTENTS

CHAPTER 1: INTRODUCTION 1

CHAPTER 2: LYOTROPIC PHASES OF BLOCK COPOLYMER-IONIC LIQUID MIXTURES IN THERMOSET RESINS 13

CHAPTER 3: BLOCK COPOLYMER PHASE EVOLUTION VIA REACTION OF THERMOSET RESINS 34

CHAPTER 4: THERMAL DECOMPOSITION OF ACYLGLYCEROLS AND THEIR CORROSIVE EFFECT ON CARBON STEEL 52

CHAPTER 5: REVERSE MICELLES OF ACYLGLYCEROL AMPHIPHILES IN NONPOLAR ALKYL ENVIRONMENTS 77

CHAPTER 6: CONCLUSION 99

CHAPTER 1: INTRODUCTION

1.1 Self-Assembly in Non-Polar Systems

Amphiphile self-assembly is ubiquitous in nature and a crucial concept in the study of soft materials. An understanding of the energetic balance that leads to spontaneous self-assembly has informed the design of whole classes of materials, from engineering composites to consumer products and drug delivery. Amphiphile self-assembly is foundational to our understanding of life – lipid self-assembly is a prerequisite to the protocells that preceded cellular organisms. Self-assembly is therefore a concept well worth studying, with implications that touch any number of subfields within materials science.

The energy/entropy balance that governs self-assembly has the natural result that in aqueous systems, there is often a strong energetic incentive available to drive self-assembly. [1] However, in systems that are non-aqueous or otherwise lack strong enthalpic interactions, more tailoring is required to identify conditions favorable to self-assembly.[2] Identifying these conditions expands the application of self-assembly towards materials design, since the usefulness of self-assembly is not limited to aqueous systems. This work describes two projects wherein self-assembly iis achieved through careful selection of composition and control of environmental factors. In addition, the phase evolution of these systems under elevated temperature is evaluated. The phase behavior is thus a complicated interplay of the thermodynamic and kinetic factors, and we attempt to rationalize our observations from theoretical understanding. These efforts expand our understanding of self-assembly in complex systems and the relevant parameters required to fabricate self-assembled materials.

1.2 Block Copolymer Self-Assembly in Reactive Thermoset systems

Block copolymers are polymers composed of distinct blocks of monomer units. They are distinguishable from other copolymers due to their block architecture, i.e. the polymer contains long runs of a single monomer and then another, rather than an alternating or random pattern. The complex phase behavior of block copolymers, even in their simplest A-B form, is a rich and insightful area of study. Flory-Huggins solution theory describes the sum of free energy contributions in a binary mixture as:

$$\Delta Gm = RT(n_1 \ln\varphi_1 + n_2 \ln\varphi_2 + n_1\varphi_2\chi_{1,2})$$

The terms n_1 and n_2 refer to the number of moles in the system, $\varphi_1$to the volume fraction, and χ to the excess free energy of mixing (i.e. the enthalpy change from an interaction between components). The additional constraint in block copolymer systems is that the two chemically dissimilar blocks are covalently linked, and thus cannot macrophase separate. In the limit of high $\chi * N$, this leads to complex self-assembly behavior on the nanoscale level. Results of these experiments have famously been shown to be remarkably consistent with theoretical predictions.[3]

The addition of a solvent has the potential to greatly complicate the phase description of a polymer system. For rigorous definition, two additional interaction χ parameters and an additional volume fraction must be introduced. However, the effect of solvent addition can be described intuitively via a "trajectory approach", first described by Handley & coworkers. [4] In the case of a diblock polymer system with a neutral solvent (that is, one with similar affinity for both blocks, the small molecule solvent simply serves to dilute the contacts between monomers, effectively reducing χ. This is equivalent to a simple downward trajectory on the phase diagram, with the assumption that the addition of solvent does not substantially change the volume

fraction parameter. In the case of a symmetric diblock, the system will simply proceed downward on the phase diagram until it reaches the order-disorder transition (ODT). For a weakly selective solvent, the trajectory will be a combination of two effects. The solvent will partially partition to both blocks, causing a simple dilution effect. However, the solvent will also partition somewhat selectively to a particular block, swelling the volume fraction of that block and moving the trajectory to the right or left. This corresponds to an overall "diagonal" movement on the phase diagram. Hanley and coworkers employed a poly(isoprene)-block-poly(styrene) polymer in their experiments. Bis(3-ethylhexyl pthaltate) (DOP) was employed as a neutral solvent selective for both blocks. Di-n-butyl phthalate (DBP) and diethyl phthalate (DEP) were employed as selective solvents for polystyrene, and are marginal and poor solvents respectively for polyisoprene. Tetradecane (C14) is a good solvent for polyisoprene but a poor solvent for polystyrene.

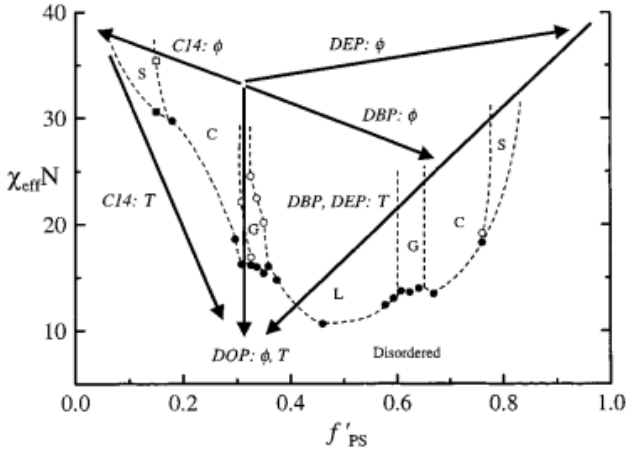

Figure 1.1: The trajectory approach to determining phase behavior of solvent-swollen block copolymer systems. DOP is a good solvent for polystyrene. DBP and DEP are good solvents for polystyrene, but marginal and poor solvents, respectively, for polyisoprene. C14 is a good solvent for polyisoprene but a poor solvent for polystyrene. From (4)

The trajectory approach is a useful framework when studying the phase behavior of certain block copolymer-modified epoxy thermosets. Block copolymer self-assembly has been

incorporated in the design of epoxy thermosets for decades, [5]and has followed one of two approaches. In the first approach, block copolymers are blended into epoxy and then cured with no change in the resulting microphase behavior. Bates & coworkers demonstrated that the classic morphologies observed in diblocks could be reproduced inside a cured epoxy thermoset under appropriate conditions.[6] The crosslinking of the surrounding epoxy (which begins as a de-facto solvent, and then transforms into high molecular weight matrix as curing progresses) kinetically traps the existing structures. In another example, Bates & coworkers (citation) demonstrated that a PEO-PEP block copolymer, blended with Bisphenol A diglicidyl ether (BADGE) epoxy, effectively toughened the materials. [7] In this approach, $\chi * N$ is initially sufficiently high to be above the order-disorder transition (ODT). In the subsequent curing reaction, $\chi * N$ only grows and thus the epoxy-phobic domain remains phase-separated. In the second approach, termed 'reaction-induced microphase separation' (RIMPS), [8, 9] the block copolymer is initially soluble in the epoxy resin. As the epoxy is cured, the changing solubility of the polymer in the matrix (i.e. the chi between epoxy resin and the polymer domains) ejects the less epoxy-soluble block from the growing epoxy network. Though initially all the components of the system are mutually soluble (and thus below the ODT on the phase diagram), as the epoxy network cures it progresses to a point above the ODT.

Using both these approaches, a wide variety of composites comprised of block copolymer, epoxy, and curing agent have been formulated. The majority have focused on formulations designed to toughen epoxy resins, and have employed traditionally used diamines as curing agents. However, restricting formulations to amine curing agents has limited the phase space, and thus the potential applications, that block-copolymer epoxy composites can traverse. The stoichiometry of the diamine-epoxy crosslinking reaction requires that the curing agent be

added to the epoxy in specific ratios, thus restricting the available compositions. Additionally, diamines cure relatively rapidly, with a pot life measured in minutes. There is no opportunity to induce a phase change through changing temperature, and then separately cure the material. A few approaches have introduced novel block copolymers, i.e. with reactive epoxy groups or groups capable of curing incorporated into the polymer structure. [10, 11] These approaches introduce additional parameters for modifying the phase behavior of the system, but the BCPs themselves are laborious to synthesize.

In this work, we have employed the use of a non-traditional curing agent – an imidazolium-based ionic liquid. Ionic liquid-cured epoxies have been shown to have comparable mechanical properties to diamine-cured epoxies. [12] However, they can be added in non-stoichiometric proportion and still obtain a cross-linked epoxy network, since their curing mechanism is a chain mechanism and not step. [13-16] Additionally, they have an extended pot life, and may be kept in a mixed formulation with epoxy for many hours at room temperature without underdoing significant reaction. Once subjected to sufficiently elevated temperature, the mixture will cure rapidly.

Ionic liquids are polar substances, and thus can easily act as selective solvents in block copolymer formulations. Thus, the microstructure of a block copolymer-ionic liquid mixture may be altered by simply varying the composition of each component. [17-19] Ionic liquids may thus be used as curing agents in a block copolymer-epoxy composite with a distinct advantage: the relative compositions of block copolymer, ionic liquid, and epoxy – and thus the microstructure of the material - can be independently varied. Ionic liquid thus may be used simultaneously as both a structure directing agent for the block copolymer and a curing agent for the epoxy.

Our work on ionic liquid-cured block copolymer epoxy can be divided into two parts. In the first, we have developed a comprehensive phase diagram of the ternary block copolymer, ionic liquid, and epoxy mixture. Binary mixtures of block copolymer and ionic liquid show a variety of diffraction peaks in small-angle x-ray scattering (SAXS), with peak locations corresponding to known classic block copolymer lyotropic phases. These phases change with the addition of epoxy resin. The changes may be rationalized via arguments regarding the relative solubility of block copolymer in ionic liquid vs. epoxy. In the second portion, a few select compositions were cured for 4 hours at 60 °C and 4 hours at 100 °C. Their subsequent phase evolution throughout the curing process was tracked via *in situ* SAXS. In one sample, extensive order-order transitions were observed with no intervening disordered phase. We rationalize the observed changes through arguments of polymer chain geometry and solubility in the curing epoxy network. This work was the first to demonstrate the variety of self-assembled nanostructures that may be achieved in epoxy resins through mixtures of block copolymer and ionic liquids.

1.3 Acylglycerol Self-Assembly in Energy Feedstock Formulations

Acylglycerols (AGs) describe a class of molecules comprised of one, two, or three fatty acids attached to a glycerol headgroup via an ester bond. These molecules, and their associated free fatty acids, have emerged as economically important replacements for petroleum feedstocks in the energy sector. Concerns regarding energy security, long-term renewability and the carbon cost of petroleum feedstocks have spurred interest in substitute feedstocks. Acylglycerols are attractive due to their mature supply chain and renewability, and have served as a crucial first-generation replacement for petroleum feeds while more advanced technologies utilizing e.g.

lignocellulose technically mature. The crucial advantage of acylglycerols is that they may be used as “drop-in” feedstocks, i.e. they can be co-refined with petroleum feedstocks without additional front-end process units or equipment upgrades. Despite the commercial success of TAGs in the energy sector, their use is currently limited by concerns regarding corrosion. TAG feedstocks have substantially different chemistry than traditional petroleum feedstocks- namely, they contain a large number of oxygen-containing moieties including esters, carboxylic acids, and alcohols. These chemical differences result in a feedstock with higher reactivity, lower thermal stability, and increased hydrophilicity than a petroleum feedstock. These features result in increased corrosiveness of the feedstocks towards process equipment.[20] Increased equipment corrosion is one of the many challenges that must be addressed as petroleum feedstocks are replaced with biofeedstocks.

The corrosivity of a feedstock is measured via its total acid number, defined as the mg of kOH required to neutralize the acids present in 1 gram of sample. [21] An unblended TAG feedstock has a wide range of possible acid numbers (e.g. 2-3 for purified soybean oil to ~80 for pyrolysis oil), but the total acid number is generally far above the industry standard of 0.5. A number of techniques have been developed to mitigate the corrosion caused by corrosive species in solution. Biofeedstocks or other inherently corrosive feedstocks are frequently blended with less corrosive species to reduce the overall TAN. Additional, capital-intensive strategies include the upgrading of process units to metallurgies less susceptible to corrosion [22, 23] or utilizing corrosion inhibitors [24] in the process. These strategies have allowed the processing of significant amounts of acylglycerol feedstocks.[25]

Acylglycerol feeds are attractive as alternatives to petroleum, but have existing competitive markets e.g. food or animal feed.[22] The next generation of biofuels seeks to utilize

feeds without an existing market, e.g. brown grease or decomposed lignocellulose, which contain more corrosive species than food-grade fats and oils. Processing these feeds requires new strategies for mitigating corrosion, ideally strategies that do not require the development of new process chemistry .

However, development of new corrosion mitigation strategies first requires more thorough understanding of how acylglycerols cause corrosion. Despite the significant commercial importance of acylglycerols, very little is known about the mechanisms by which they cause corrosion. As a result, there is little understanding of which factors affect the corrosion process. These factors may be inherent to the process (e.g. the chemistry between a chosen feedstock-metal combination) or external and modifiable (e.g. temperature). This is a crucial gap in understanding that becomes more significant as refiners seek to lower the carbon cost of their feedstocks and products. [20] Without insight into the factors that affect corrosion, refiners are operating without knowledge of their process limits. Thus, they risk operating at either sub-optimal efficiencies or at conditions which reduce equipment lifetime.

Our work on acylglycerol self-assembly can be divided into two portions. In the first portion, we perform systematic high-temperature corrosion experiments with a model system comprised of biofeedstock blends and metal coupons. This work provides crucial insights into the reactions between an acylglycerol and steel. By performing these experiments under elevated temperature and pressure, we provide an accelerated picture of reactions that may occur under process conditions. In the second portion, we design reverse-micelle forming acylglycerol mixture informed by the results of the first portion. These mixtures are designed to be less corrosive than mixtures lacking reverse micelles, due to the tendency of polar species to sequester within the polar core of a reverse micelle. We utilize species expected to be generated

during the thermal reactions of acylglycerols, e.g. monoglycerides, water, and fatty acids. By exploiting the amphiphilic nature of monoglycerides, we demonstrate that reverse micelles can be formed by appropriate mixtures of monoglycerides in white mineral oil, and that fatty acids and polar solvents may be incorporated into solution while keeping the micelle intact. We hope to lay the groundwork for the design of biofeedstock mixtures that neutralize corrosive species by designing mixtures that sequester the more corrosive (i.e. more polar) species.

References

1. Israelachvili JN, Mitchell DJ, Ninham BW. Theory of self-assembly of hydrocarbon amphiphiles into micelles and bilayers. *J Chem Soc Faraday Trans 2 Mol Chem Phys*. 1976;72:1525-1568. doi:10.1039/F29767201525
2. Correa NM, Silber JJ. On the Formation of New Reverse Micelles: A Comparative Study of Benzene/Surfactants/Ionic Liquids Systems Using UV-Visible Absorption Spectroscopy and Dynamic Light Scattering. :1-13.
3. Bates FS, Fredrickson GH. Block copolymers-designer soft materials. *Phys Today*. 1999;52(2):32-38. doi:10.1063/1.882522
4. Hanley KJ, Lodge TP, Huang CI. Phase behavior of a block copolymer in solvents of varying selectivity. *Macromolecules*. 2000;33(16):5918-5931. doi:10.1021/ma000318b
5. Hillmyer MA, Lipic PM, Hajduk DA, Almdal K, Bates FS. Self-assembly and polymerization of epoxy resin-amphiphilic block copolymer nanocomposites. *J Am Chem Soc*. 1997;119(11):2749-2750. doi:10.1021/ja963622m
6. Lipic PM, Bates FS, Hillmyer MA. Nanonstructured thermosets from self-assembled amphiphilic block copolymer/epoxy resin mixtures. *J Am Chem Soc*. 1998;120(35):8963-

8970. doi:10.1021/ja981544s

7. Wu J, Thio YS, Bates FS. Structure and properties of PBO-PEO diblock copolymer modified epoxy. *J Polym Sci Part B Polym Phys*. 2005;43(15):1950-1965. doi:10.1002/polb.20488

8. Guo Q, Thomann R, Gronski W, Thurn-Albrecht T. Phase behavior, crystallization, and hierarchical nanostructures in self-organized thermoset blends of epoxy resin and amphiphilic poly(ethylene oxide)-block-poly(propylene oxide)-block-poly(ethylene oxide) triblock copolymers. *Macromolecules*. 2002;35(8):3133-3144. doi:10.1021/ma011971h

9. Parameswaranpillai J, Hameed N, Pionteck J, Woo EM. *Handbook of Epoxy Blends*.; 2017. doi:10.1007/978-3-319-40043-3

10. Grubbs RB, Dean JM, Broz ME, Bates FS. Reactive block copolymers for modification of thermosetting epoxy. *Macromolecules*. 2000;33(26):9522-9534. doi:10.1021/ma001414f

11. Hameed N, Guo Q, Xu Z, Hanley TL, Mai YW. Reactive block copolymer modified thermosets: Highly ordered nanostructures and improved properties. *Soft Matter*. 2010;6(24):6119-6129. doi:10.1039/c0sm00480d

12. Hanze AR, Conger TW, Wise EC, Weisblat DI. Room Temperature Ionic Liquids as Thermally Latent Initiators for Polymerization of Epoxy Resins. *Macromolecules*. 2009;42(9):3219-3221. doi:10.1021/ja01211a087

13. Binks FC, Cavalli G, Henningsen M, Howlin BJ, Hamerton I. Investigating the mechanism through which ionic liquids initiate the polymerisation of epoxy resins. *Polymer (Guildf)*. 2018;139:163-176. doi:10.1016/j.polymer.2018.01.087

14. Carvalho APA, Santos DF, Soares BG. Epoxy/imidazolium-based ionic liquid systems: The effect of the hardener on the curing behavior, thermal stability, and microwave

absorbing properties. *J Appl Polym Sci*. 2020;137(5):1-11. doi:10.1002/app.48326

15. Jiang Z, Wang Q, Liu L, Zhang Y, Du F, Pang A. Dual-Functionalized Imidazolium Ionic Liquids as Curing Agents for Epoxy Resins. *Ind Eng Chem Res*. 2020;59(7):3024-3034. doi:10.1021/acs.iecr.9b06574
16. Ropital F. Current and future corrosion challenges for a reliable and sustainable development of the chemical, refinery, and petrochemical industries. *Mater Corros*. 2009;60(7):495-500. doi:10.1002/maco.200805171
17. Virgili JM, Hexemer A, Pople JA, Balsara NP, Segalman RA. Phase behavior of polystyrene-block-poly(2-vinylpyridine) copolymers in a selective ionic liquid solvent. *Macromolecules*. 2009;42(13):4604-4613. doi:10.1021/ma900483n
18. Virgili JM, Hoarfrost ML, Segalman RA. Effect of an ionic liquid solvent on the phase behavior of block copolymers. *Macromolecules*. 2010;43(12):5417-5423. doi:10.1021/ma902804e
19. Virgili JM, Nedoma AJ, Segalman RA, Balsara NP. Ionic liquid distribution in ordered block copolymer solutions. *Macromolecules*. 2010;43(8):3750-3756. doi:10.1021/ma9027307
20. Marker T. *Opportunites for Biorenewables in Oil Refineries*. Vol DE-FG36-05.; 2005.
21. ASTM. *American Society of Testing and Materials: Annual Book of Standards*.; 2019. doi: 10.1520/D0664-18E02.
22. Tyson KS, Bozell J, Wallace R, Petersen E, Moens L. Biomass Oil Analysis : Research Needs and Recommendations Biomass Oil Analysis : Research Needs and Recommendations. *Contract*. 2004;(June):116. http://oai.dtic.mil/oai/oai?verb=getRecord&metadataPrefix=html&identifier=A

DA435922.

23. Shetty PP, Daryadel S, Haire BT, et al. Low-Temperature Pack Aluminization Process on Pipeline Steel to Inhibit Asphaltene Deposition. *ACS Appl Mater Interfaces*. 2019;11(50):47596-47605. doi:10.1021/acsami.9b17430

24. Zhu Y, Free ML, Woollam R, Durnie W. A review of surfactants as corrosion inhibitors and associated modeling. *Prog Mater Sci*. 2017;90:159-223. doi:10.1016/j.pmatsci.2017.07.006

25. Sergios K, van Dyk JS, McMillan J, Saddler J. Drop-in biofuel production via conventional (lipid/fatty acid) and advanced (biomass) routes. Part I. *Biofuels, Bioprod Biorefining*. 2017;11:344-362. doi:https://doi.org/10.1002/bbb.1746

CHAPTER 2: LYOTROPIC PHASES OF BLOCK COPOLYMER-IONIC LIQUID MIXTURES IN THERMOSET RESINS

2.1 Introduction

Epoxy resins are extensively used as high-performance polymeric materials.[1] The high modulus, low creep, and chemical resistance [2] of highly crosslinked epoxy networks mean they are useful in a variety of applications, from construction adhesives [3-5] to aerospace composites. [6-8] The key failure of epoxies is their relatively brittle nature, with poor resistance to crack initiation and propagation. Composite epoxy formulations have sought to overcome that limitation, with various additives blended in to increase toughness. Some successful formulations have incorporated a secondary polymer phase into the resin, [1,9] which increase the toughness without significantly compromising other properties.

Block copolymers (BCPs) have been shown to be one of the most effective epoxy toughening agents.[10-14] A block copolymer with both epoxy-phobic and epoxy-philic domains will form self-assembled micelles within the epoxy resin, with the epoxy-phobic domain phase separating to form a minority phase. These micelles may have various geometries, including spherical [15] or wormlike. [10] The specific configuration of the block copolymer within the resin is guided by the same principles governing BCPs in selective solvents. The nanostructures are highly dependent on the free energy interactions between BCP components, epoxy monomers, and the curing agents. Careful control of these nanostructures is essential for optimizing the mechanical and functional properties of these epoxy/BCP blends.

A few pieces of work have demonstrated that BCP-epoxy composites may have significant potential beyond being utilized as toughened, high-performance materials. Bates, *et al.* demonstrated that with appropriate selection of BCP, epoxy, and hardener, the classical

phases observed in a BCP diblock melt may be observed in the resin. [16] Thus, a cross-linked epoxy matrix may have well-ordered, nanoscopic features comprised of block copolymer domains. A variety of nanostructures have been demonstrated in BCP-epoxy blends, including disordered spherical micelles [17], wormlike micelles [10], and vesicles [18] as well as ordered structures- for example, spheres on a body centered-cubic (BCC) lattice, hexagonally packed cylinders, and lamellar morphologies. [19,20] Additionally, it is well known that block copolymers can be enormously successful templating agents [21] for appropriately functionalized inorganic nanoparticles. Thus, with appropriate component selection, epoxy resins may be functionalized with a nanoparticle of choice, with the nanoparticle appropriately distributed as determined by the block copolymer phases.

There are two primary mechanisms for the formation of nanostructures in epoxy/BCP blends: self-assembly and reaction-induced microphase separation (RIMPS). [20,22] In both cases, the structures are the result of the relative miscibility of the BCP polymer blocks in the epoxy resin, where the less miscible block forms the nanophase-separated domains and the more miscible block concentrates in the epoxy phase. In the self-assembly mechanism, the epoxy-phobic block immediately phase separates from the epoxy resins, while the epoxy-philic block is dissolved in the uncured resin. The curing process kinetically traps pre-existing structures. [23-26] For RIMPS, both blocks are initially miscible in the epoxy resin, but as the epoxy begins to cure, one of the blocks is expelled from the growing network and nanophase separates. [15, 27-29]

In this work, we demonstrate a new approach to formulating epoxy networks with nanoscopic features. Most work in this space employs some variation on a Bisphenol A-type epoxy with a diamine curing agent.[14] We have instead utilized an ionic liquid (IL)-type curing

agent, specifically 1-ethyl 3-methyl imidazolium dicyanamide (EMIM-DCA). By simple variation of the relative fraction of the block copolymer, epoxy, and curing agent, we demonstrate via small-angle x-ray scattering (SAXS) experiments that lamellar, disordered sphere, body centered cubic (BCC) sphere, and hexagonally packed cylinder phases can be observed within the uncured epoxy matrix.

Ionic liquids have number of interesting applications, and a body of work exists on modifying block copolymers with various ILs. Ionic liquids are unusual solvents in that they are comprised entirely of ionic compounds with low lattice energy (and thus low melting points). They are unusually thermally stable for organic solvents, with low vapor pressure, and are thus attractive for applications where volatile organic compound (VOC) emission or solvent recyclability may be a concern. Ionic liquids possess excellent conductivity and thus have been employed as additives in the design of many materials, e.g. fuel cells and battery electrolytes.

Ionic liquids were first shown to be effective solvents for forming amphiphilic block copolymer solutions in the 1980s, utilizing derivatives of ammonium nitrate. [30] The same fundamental solvophobic effect that governs self-assembly in water is also thought to apply in ionic liquids. Ionic liquids have also been shown to be effective block copolymer phase modifiers for concentrated, melt-like polymer solutions. [31-33] Upon the addition of a selective solvent to a diblock melt system, one phase is preferentially swelled by the solvent. This simultaneously changes both the volume fraction of the blocks and the effective degree of segregation between the blocks, χ_{eff}. When this phenomenon is coupled with the additional functionality imparted by ionic liquids (e.g. electrical or ionic conductivity), modifying BCPs with ionic liquids emerges as an intriguing strategy for designing functionalized BCP materials. For instance, Segalman & Hoarfrost designed poly(styrene)-b-poly(2-vinyl pyridine) BCP

membranes incorporating two different ionic liquids into the BCP to create a conductive polymer membrane.[34] IL-modified polymers have also been explored as battery electrolytes [35] and capacitor materials.[36]

To our knowledge, our published work is the first demonstration of lyotropic block copolymer phases modified by ionic liquid **within an epoxy matrix.** We utilize a few block copolymers in our work. The most extensive work was done with an ubiquitous and commercially available BCP, Pluronic P123. This BCP is comprised of three blocks, poly(ethylene oxide-b-propylene oxide-b-ethylene oxide) (PEO–PPO–PEO). While P-123 has been utilized in toughening epoxy/BCP blends, the nanostructure of the blends have been mostly limited to disordered spherical micelles formed through the RIMPS mechanism. [37-39] Here, we show that the classic diblock phases may be observed via self-assembly at appropriate concentrations. In addition, we show data corresponding to low concentrations of poly(ethylene-alt-propylene-b-ethylene oxide) (PEP-PEO), and poly(isoprene-b-ethylene oxide) (PI-PEO). For PEP-PEO, strong structure factor scattering with well-defined d-spacing was observed, overlaid on form factor scattering consistent with spherical scattering domains. PI-PEO demonstrates similar features, but with a few compositions showing structure factor scattering corresponding to the classic diblock phases.

2.2 Materials & Methods

Materials

Bisphenol A diglycidyl ether (BADGE), 1-ethyl 3-methyl imidazolium dicyanamide (EMIM-DCA) ionic liquid (IL) (98%), and poly(ethylene oxide-b-propylene oxide-b-ethylene oxide) (PEO20–PPO70–PEO20) (Pluronic, P-123, MW ~5,800 g/mol) were purchased from

Sigma-Aldrich and used without further purification. Additional polymers, poly(ethylene-alt-propylene-b-ethylene oxide (PEP95-PEO375) and poly(1,4 isoprene 95 -b-ethylene oxide (PI95-PEO375) were obtained from PolymerSource and used as received. PDI for PI-PEO and PEP-PEO polymers is 1.04.

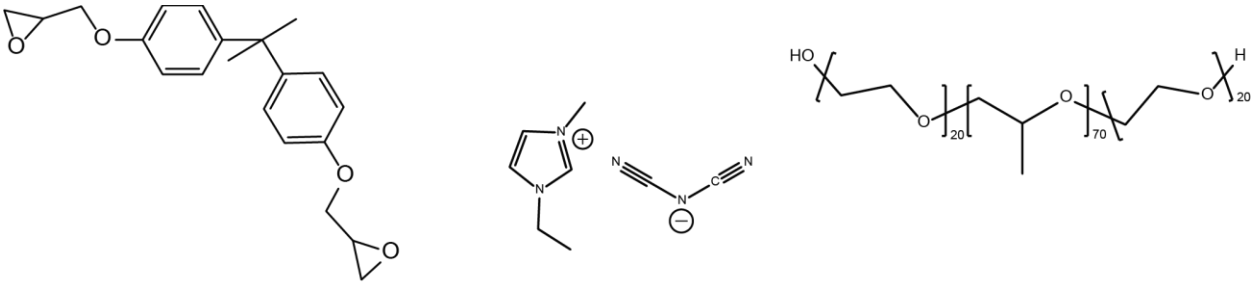

Scheme 2.1: Molecular structure of some materials used in this work

Preparation of Samples

Polymer and IL were added to a mixing cup and heated between 60 and 70 °C until the polymer was fully melted. The sample was then mixed at 2000 rpm for 2 min using a FlakTek SpeedMixer. This mixture was cooled to room temperature after mixing. Subsequently, BADGE was added, and the blend was mixed at 2000 rpm for another 2 min in the SpeedMixer. For small-angle X-ray scattering (SAXS) experiments, the blends were loaded into a 1.5 mm quartz glass capillary using a syringe with a long 22 Ga needle.

Small-Angle X-ray Scattering

SAXS was mostly performed using a custom-built beamline at the Materials Research Laboratory at the University of Illinois at Urbana-Champaign. The beamline employs a Cu- Kα

X-ray source at 50 keV and a high-speed Pilatus 300 detector. A few experiments were performed at the Advanced Photon Source at Argonne National Laboratory at beamline 12-BM-B. In both cases, two -dimensional scattering data were collected and azimuthally averaged to generate a 1D plot of scattered intensity versus q, where q is the scattering wave vector. Data was analyzed using a combination of custom Matlab scripts and Fit2D.

2.3 Ternary phase diagrams of ionic liquid, block copolymer and uncured epoxy resin

Blends of EMIM-DCA, P-123, and BADGE were prepared as described in the methods section and evaluated via SAXS to identify the morphology of the self-assembled structures. EMIM-DCA IL plays a critical role in driving self-assembly of P-123 BCPs, which is seen when this result is compared with existing results reported for other epoxy/PEO–PPO–PEO blends.[19] A wide variety of compositions were tested, and a ternary phase diagram for the P-123 structures in the uncured epoxy blends was developed (Figure 2.1).

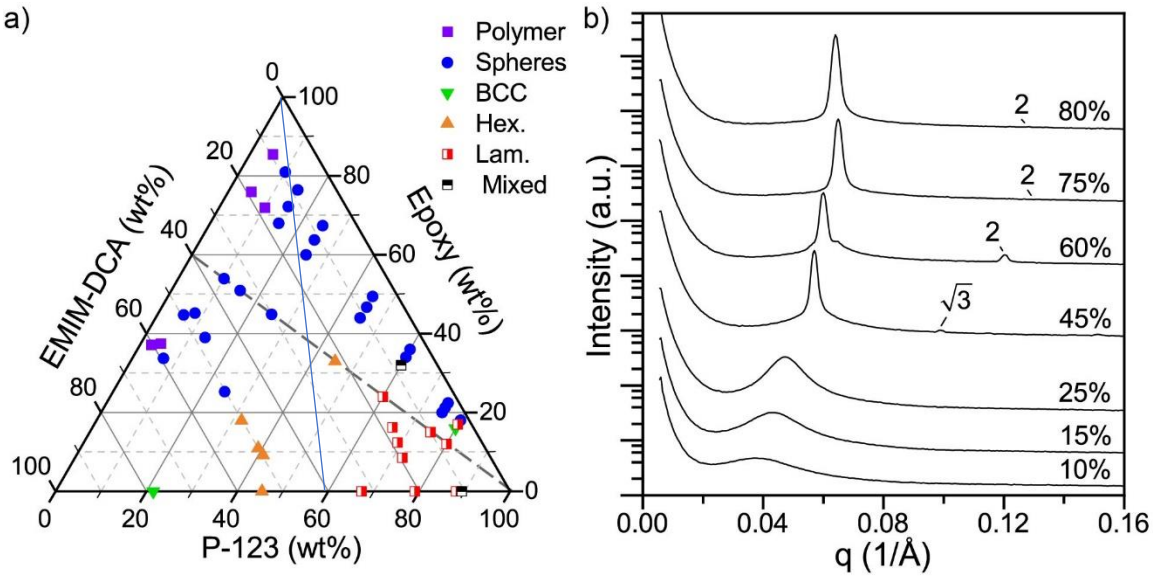

Figure 2.1. *(a)* Ternary phase diagram developed for the uncured blends of epoxy, EMIM-DCA, and P-123 as determined using SAXS. The grey dashed diagonal line indicates a line of equal ratio epoxy/EMIM-DCA (1.5:1) The solid blue line indicates a line of equal ratio

Figure 2.1 (cont.). polymer/EMIM-DCA (1.5:1) *b)* Representative SAXS traces are shown for the compositions along the dashed line. Labels indicate the P-123 wt %. Peak labels indicate the ratio of the peak position to the primary peak position. Line scans are shifted vertically for clarity.

These data showed that P-123 can self-assemble into a variety of classically observed BCP structures including disordered spherical micelles, hexagonally packed cylindrical micelles, and lamellar structures. Additional dissolved polymer (no features in SAXS) and mixed (combined hex/lam) phases were observed. A more detailed look at the phase space identifies several important features. First, no structure was observed in the SAXS data for the uncured epoxy/P-123 binary blends, indicating that both blocks of the P-123 BCP are fully dissolved in the epoxy monomers. This result is consistent with previously published results. [13,37] Additionally, there were several ternary compositions with low P-123 concentration (<5 wt %) that also showed no structure, designated as "polymer" in Figure 2.1. However, this dissolved polymer region of the phase diagram was relatively small. Minor changes to the compositions resulted in the self-assembly of disordered micelles, as was indicated by a diffuse primary peak in the SAXS data. For the spherical micelles, the PPO blocks nanophase separate and form the micelle core, while the PEO blocks form the corona with the chains miscible in the epoxy/EMIM-DCA matrix phase. Based on the q value of the peak maximum, these micelles have an estimated spacing ranging from 9 to 22 nm (Figure 2.2)

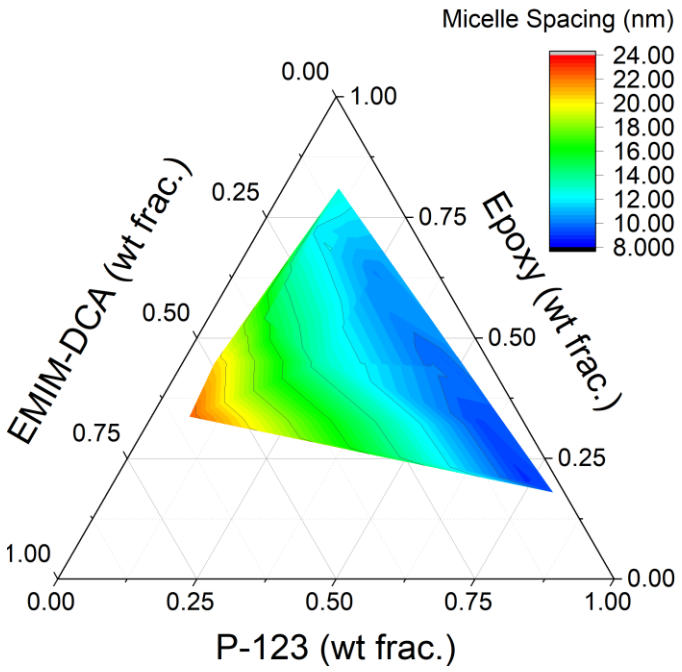

Figure 2.2: Estimated micelle spacing based on location of the primary peak maximum intensity in SAXS data.

At higher concentrations of EMIM-DCA and P-123, higher order Bragg peaks corresponding to hexagonally packed cylindrical micelles and lamellar phases are present in the SAXS data. The phase transitions as a result of increased P-123 concentration can be seen in Figure 2.1b for the compositions with a 1.5:1 ratio of epoxy/EMIM-DCA. The presence of these self-assembled, long-range ordered structures is somewhat surprising since P-123 is a relatively short and polydisperse BCP. Generally, the appearance of an unambiguous structure factor requires long, low polydispersity polymers. [40] To our knowledge, there are no examples in the literature of epoxy/PEO–PPO–PEO blends with ordered structures in the uncured state. [19,22] In this case, we have simply mixed P-123 (a ubiquitous and commercially available BCP) together with other commercially available components to drive the self-assembly of the highly ordered structures.

These results indicate that the IL acts as a selective solvent to the PEO block and drives BCP self-assembly, a result more rigorously demonstrated in the next section. This result is consistent with the use of IL as an amphiphile selective solvent in a number of applications. [30]

2.4 Determination of ionic liquid selective solvent behavior

The selectivity of a solvent for block copolymer domains may be assessed by employing the scaling relationship $d \sim \Phi^{\alpha}$, derived from self-consistent mean field theory [41], where d is the principal domain spacing and Φ is the volume fraction of polymer. The value of α may be used as a descriptor of the selectivity of the solvent. In the case of a neutral solvent, $\alpha = 1/3$. [42] This may be intuitively understood by visualizing the neutral solvent particles as "screening" A-B contacts, or reducing the effective enthalpic cost of an A-B interaction, $\chi_{AB,eff}$. This reduces the cost of an interface and thus shrinks the d-spacing vs. the melt state, as chains orient away from the direction normal to the interface. If $\alpha = 0$, the addition of solvent has no effect on $\chi_{AB,eff,}$ and no change in d-spacing is observed as polymer volume fraction is changed. If $\alpha < 0$, the solvent selectively swells the block copolymer such that chain stretching normal to the interface dominates parallel stretching. A greater α magnitude corresponds to increased selectivity and thus greater d-spacing.

The value of α, and thus a measure of solvent selectively, may be extracted by plotting d vs. Φ on a log-log scale. This analysis may be employed for the region of the phase diagram corresponding to 0% epoxy to identify the solvent behavior of ionic liquid towards P-123 (Figure 2.3). It is apparent that for the 4 lamellar phases (including the mixed hex/lam phase at high polymer content), the location of the primary peak systematically shifts towards lower q (or higher d-spacing).

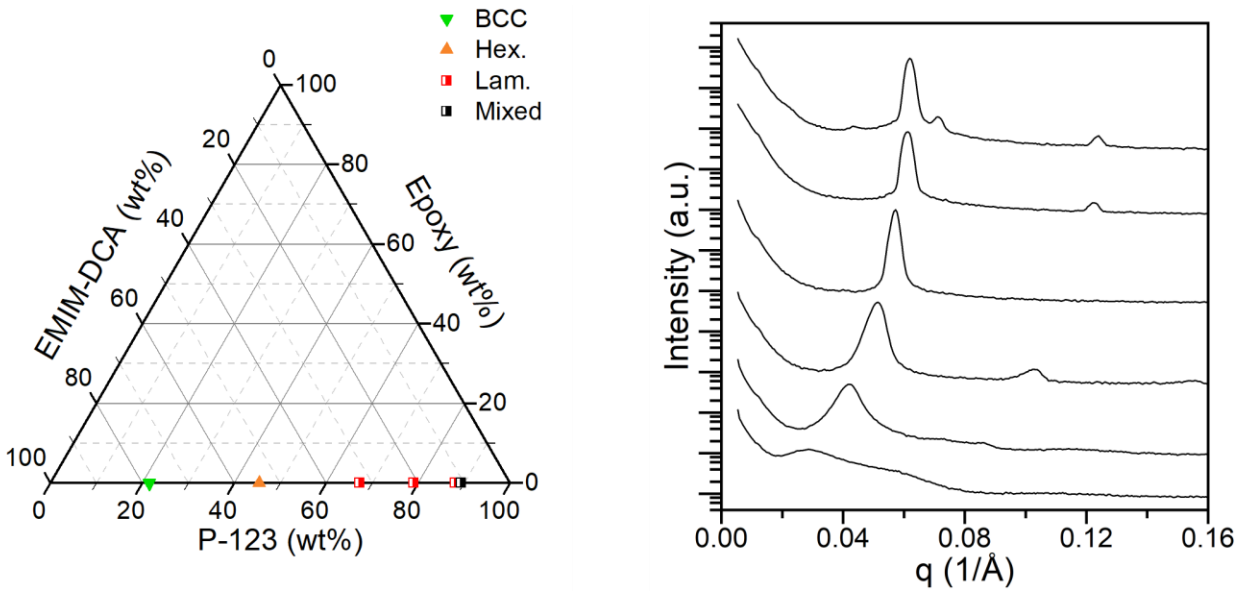

Figure 2.3: Region of the phase diagram corresponding to 0% epoxy, with corresponding SAXS linescanes. SAXS is shown in order of increasing polymer content, from top to bottom.

Graphing d versus $\Phi_{polymer}$ for the lamellar phases yields a slope of $\alpha = -0.61$ (Figure 2.4), the negative value indicating that EMIM-DCA is a strong selective solvent for P-123. This α is unusually low when compared to typical pairings of polymer with molecular solvents, [42] but a typical value for ionic liquids. [33] Though we have not rigorously shown that the EMIM-DCA partitions to the PEO over the PPO, the relative polarity of PEO over PPO suggests that EMIM-DCA is more likely to partition to the PEO block. The tendency of an ionic species to selectively partition to the more polar block of a BCP, and thus act to increase the segregation strength between blocks and drive BCP self-assembly, is well established. [32,33,43]

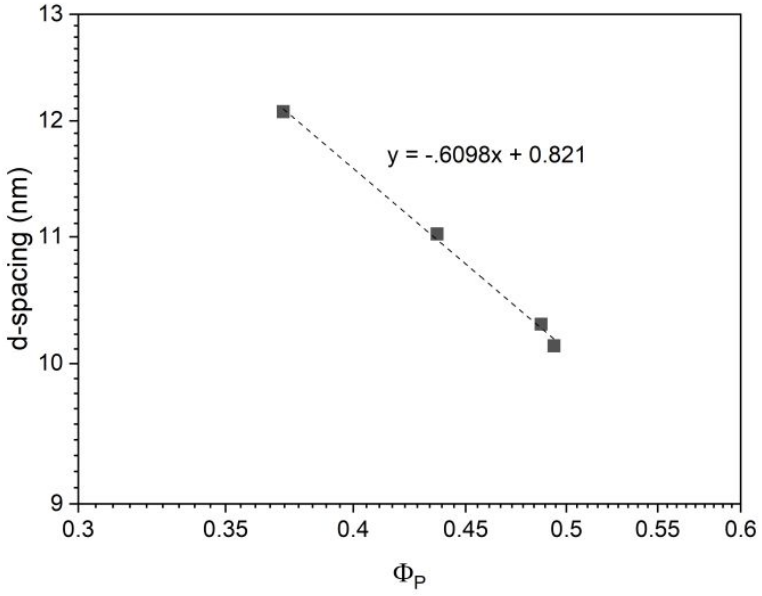

Figure 2.4: Primary domain spacing d is plotted against Φ, polymer volume fraction. The value of α is the slope of the fitted curve.

The assertion that EMIM-DCA is a selective solvent for P-123 is consistent with the observed phase changes from low to high ionic liquid in Figure 2.1a at fixed ratio of EMIM-DCA:P-123. As ionic liquid is added, $\chi_{AB,eff}$ increases, thus increasing the energetic cost of an A-B interface. At sufficiently high ionic liquid content, phase transitions are observed which seek to minimize interfacial A-B contacts.

2.5 BADGE epoxy as a neutral solvent for IL-modified P-123

The same principles governing selective solvent vs neutral solvent behavior may be employed to elucidate the behavior of BADGE epoxy towards the IL-modified polymer system. This maybe be visualized by following the solid blue line in Figure 2.1a, which corresponds to a line of fixed IL:polymer ratio. Moving up along the line is thus the equivalent of dilution of an existing phase by epoxy. Phase transitions progressing from higher to lower interfacial area are observed, suggesting that the addition of epoxy is behaving as a neutral solvent according to the

principles outlined above – the addition of epoxy effectively reduces the free energy cost of an interface.

2.6 Other polymers

In addition to the P-123 examined in the previous sections, two additional polymers – PEP-PEO, and PI-PEO, were examined. 2-D SAXS is shown in Figure 2.5 for PEP-PEO for two data sets. Figure 2.5a shows a series with increasing polymer content, with a fixed ratio of EMIM-DCA/epoxy of 1:.5.7. Figure 2.5b shows a fixed ratio of EMIM-DCA/epoxy of 1:1.5. In both cases, the scattering qualitatively resembles spherical form factor scattering combined with structure factor peaks, with the structure factor weakening as the amount of polymer decreases.

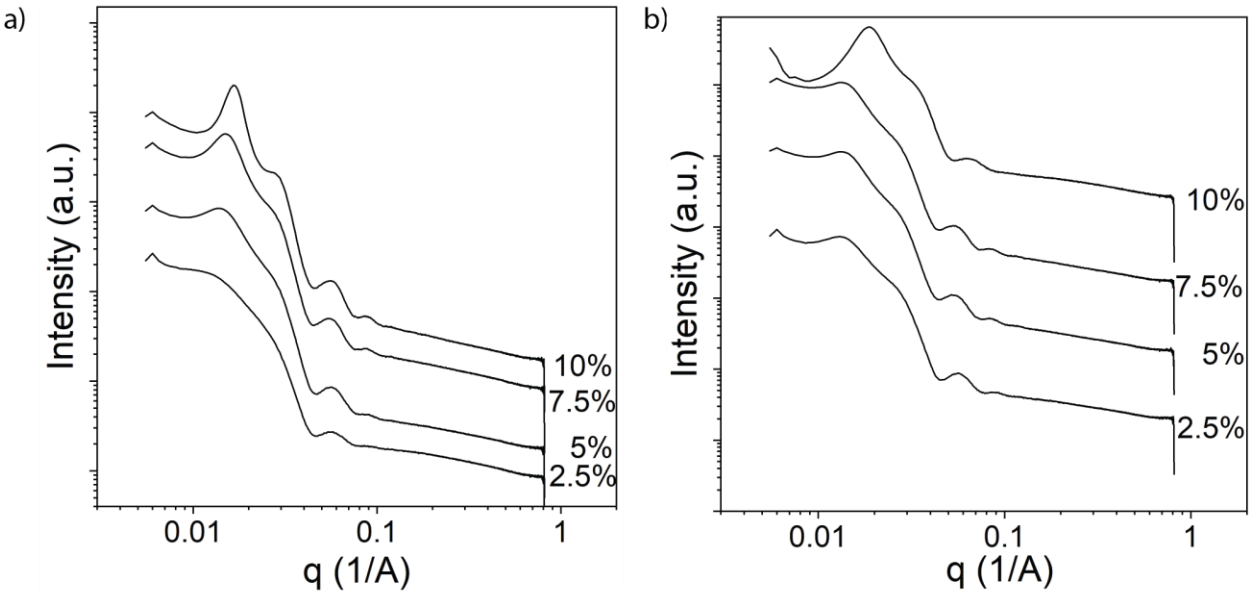

Figure 2.5: 2-D SAXS linescans for PEP-PEO at various polymer concentrations a) Linescans for a ratio of EMIM-DCA:epoxy of 0.15:0.85. b)Linescans for a ratio of EMIM-DCA:epoxy of 11.5

Figure 2.6a shows calculated models from dilute scattering from spherical form factors overlaid on experimental data with capillary background subtracted. The experimental data corresponds to a sample containing 10 wt% PEP-PEO, with the balance a mixture of EMIM-

DCA and epoxy in a ratio of 1:5.7 (Figure 2.6a) or 1:1.5 (Figure 2.6b). Although the Bessel oscillation of the sphere scattering fits the experimental data in the mid-q range, the presence of a structure factor peak indicates that the assumption of dilute spheres is incorrect. This explains the significant deviation from the model at low q. The rational for deviation from high q is less clear, but the origin may be excess background scattering from the epoxy solvent. The overall trend of the data indicates that PEP-PEO within an IL-epoxy matrix is forming spherical domains, with the d-spacing between spherical domains becoming increasingly well defined as polymer concentration increases. The effect of ionic liquid is minimal for the purposes of modifying phase behavior in this PEP-PEO system, as the model parameters are quite similar between the two samples.

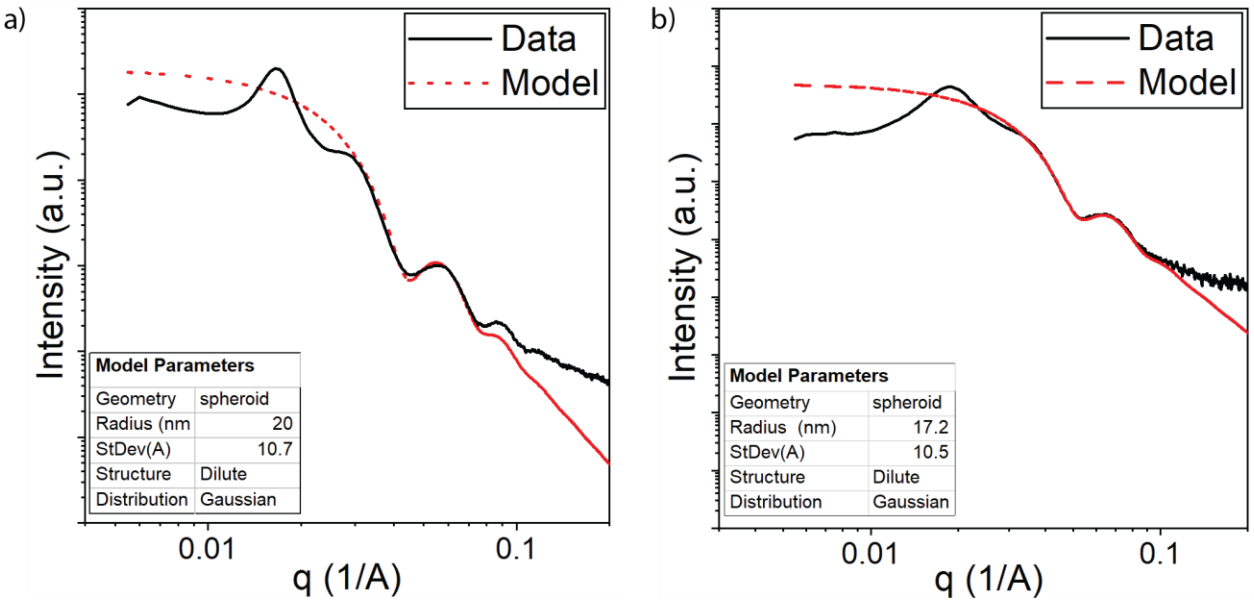

Figure 2.6: Experimental data (10 wt% PEP-PEO) with a calculated model of spherical form factor SAXS scattering. *a)* EMIM-DCA:epoxy of 1:5.7. *b)* EMIM-DCA:epoxy of 1:1.5

2-D SAXS linescans for PI-PEO are shown in Figure 2.7. The same strong form factor scattering, overlaid onto structure factor scattering, also appears in this experimental set. Figure

2.7a corresponds to PI-PEO blended with an epoxy mixture of EMIM-DCA:epoxy of 1:5.7 and Figure 2.7b a ratio of EMIM-DCA:epoxy of 1:1.5. However, a few compositions show higher order structure factor peaks. Interestingly, in this case there is a distinct change between the phases observed at low and high ionic liquid content. Since poly(isoprene) is relatively more polar than poly(ethylene-alt-propylene), a difference in interactions between the ionic liquid and the alkyl polymer may be the basis of this difference in phase behavior.

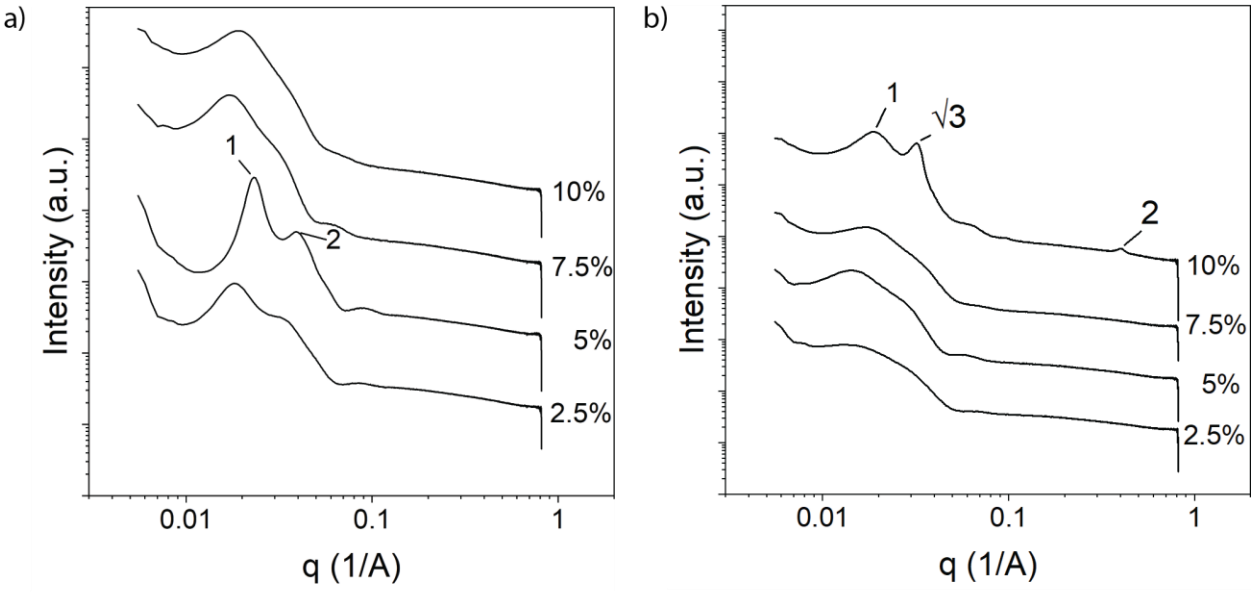

Figure 2.7: 2-D SAXS linescans for PI-PEO at various polymer concentrations *a)* Linescans for a ratio of EMIM-DCA:epoxy of 1:5.7. *b)* Linescans for a ratio of EMIM-DCA:epoxy of 1:1.5

2.7 Conclusions & Outlook

In this section, we have shown that ionic liquids are effective phase modifiers for block copolymers in epoxy solutions. Ionic liquids act as selective solvents in the case of the small polymer, Pluronic P-123, and are sufficient to modify the phase behavior when added in appropriate amounts. Significantly, lyotropic phases with multiple structure factor peaks in SAXS (corresponding to long-range order) are observed by simply blending together P-123,

epoxy, and ionic liquid. The classic diblock phases were observed at a variety of concentrations in a full ternary phase diagram. Structure factor scattering and form factor scattering were both observed in low-concentration solutions of PEP-PEO and PI-PEO with ionic liquid and epoxy. Ionic liquid modified the phase behavior of PI-PEO solutions, but only d-spacing changes were observed for PEP-PEO.

Taking advantage of the superior mechanical properties of epoxy requires that block copolymer and hardener remain the majority phase in any epoxy composite formulations. Our work in this section demonstrated that phases other than simple spheres require relatively high concentrations of polymer and/or ionic liquid, which potentially compromise the epoxy matrix. However, the emergence of unambiguous structure factor peaks and well-defined d-spacing of the spherical phases at low polymer concentrations indicates that the polymer domains are well-dispersed in the spherical phase. In addition, the PI-PEO and PEP-PEO polymers exhibited phase transitions at relatively low weight percent. This suggests that complex block copolymer phase behavior, in relatively low concentrations in epoxy, is achievable. The well-defined d-spacing exhibited by the polymer phases in this work suggest that they are prime candidates for the templating of nanoparticles (which have the primary requirement that polymer domains are well-separated to prevent excessive aggregation).

The great advantage of block copolymers is the sheer variety of chemistries and architectures available to the experimentalist. In this work we have employed relatively simple, linear block copolymers to elucidate the fundamental principles that guide the phase behavior in these kinds of formulations. Future work may draw on the rich variety of block copolymers as epoxy additives, with the expectation that already complex phase behavior will be further modified by the addition of ionic liquids.

Portions of this text are modified from previously published work.

Liu, D & Krogstad, D. V. Self-Assembly and Phase Transformation of Block Copolymer Nanostructures in Ionic-Liquid Cured Epoxy. Macromolecules 2021, 54, 2, 988–994. doi.org/10.1021/acs.macromol.0c02214

References

1. Jose S, George SM. Handbook of Epoxy Blends. *Handb Epoxy Blends*. 2015. doi:10.1007/978-3-319-18158-5
2. Cooke HG. Chemical resistance of epoxy resins. *Ind Eng Chem*. 1964;56(5):38-41. doi:10.1021/ie50653a005
3. Banea MD, De Sousa FSM, Da Silva LFM, Campilho RDSG, De Pereira AMB. Effects of temperature and loading rate on the mechanical properties of a high temperature epoxy adhesive. *J Adhes Sci Technol*. 2011;25(18):2461-2474. doi:10.1163/016942411X580144
4. de Morais AB, Pereira AB, Teixeira JP, Cavaleiro NC. Strength of epoxy adhesive-bonded stainless-steel joints. *Int J Adhes Adhes*. 2007;27(8):679-686. doi:10.1016/j.ijadhadh.2007.02.002
5. Sousa JM, Correia JR, Cabral-Fonseca S. Durability of an epoxy adhesive used in civil structural applications. *Constr Build Mater*. 2018;161:618-633. doi:10.1016/j.conbuildmat.2017.11.168
6. Toldy A, Szolnoki B, Marosi G. Flame retardancy of fibre-reinforced epoxy resin composites for aerospace applications. *Polym Degrad Stab*. 2011;96(3):371-376. doi:10.1016/j.polymdegradstab.2010.03.021
7. Guadagno L, Raimondo M, Vittoria V, et al. Development of epoxy mixtures for

application in aeronautics and aerospace. *RSC Adv*. 2014;4(30):15474-15488. doi:10.1039/c3ra48031c

8. Jakubinek MB, Ashrafi B, Zhang Y, et al. Single-walled carbon nanotube-epoxy composites for structural and conductive aerospace adhesives. *Compos Part B Eng*. 2015;69:87-93. doi:10.1016/j.compositesb.2014.09.022
9. Toughening RP, Resins E. Rubbery and Rigid Particle Toughening. :177-189.
10. Liu J, Thompson ZJ, Sue HJ, et al. Toughening of epoxies with block copolymer micelles of wormlike morphology. *Macromolecules*. 2010;43(17):7238-7243. doi:10.1021/ma902471g
11. Li T, He S, Stein A, Francis LF, Bates FS. Synergistic Toughening of Epoxy Modified by Graphene and Block Copolymer Micelles. *Macromolecules*. 2016;49(24):9507-9520. doi:10.1021/acs.macromol.6b01964
12. Wu J, Thio YS, Bates FS. Structure and properties of PBO-PEO diblock copolymer modified epoxy. *J Polym Sci Part B Polym Phys*. 2005;43(15):1950-1965. doi:10.1002/polb.20488
13. Chu WC, Lin WS, Kuo SW. Flexible epoxy resin formed upon blending with a triblock copolymer through reaction-induced microphase separation. *Materials (Basel)*. 2016;9(6). doi:10.3390/ma9060449
14. Ruiz-Pérez L, Royston GJ, Fairclough JPA, Ryan AJ. Toughening by nanostructure. *Polymer (Guildf)*. 2008;49(21):4475-4488. doi:10.1016/j.polymer.2008.07.048
15. Meng F, Zheng S, Zhang W, Li H, Liang Q. Nanostructured thermosetting blends of epoxy resin and amphiphilic poly(ε-caprolactone)-block-polybutadiene-block-poly(ε-caprolactoné) triblock copolymer. *Macromolecules*. 2006;39(2):711-719.

doi:10.1021/ma0518499

16. Lipic PM, Bates FS, Hillmyer MA. Nanonstructured thermosets from self-assembled amphiphilic block copolymer/epoxy resin mixtures. *J Am Chem Soc*. 1998;120(35):8963-8970. doi:10.1021/ja981544s

17. Meng F, Zheng S, Li H, Liang Q, Liu T. Formation of ordered nanostructures in epoxy thermosets: A mechanism of reaction-induced microphase separation. *Macromolecules*. 2006;39(15):5072-5080. doi:10.1021/ma060004+

18. Ritzenthaler S, Court F, David L, Girard-Reydet E, Leibler L, Pascault JP. ABC triblock copolymers/epoxy-diamine blends. 1. Keys to achieve nanostructured thermosets. *Macromolecules*. 2002;35(16):6245-6254. doi:10.1021/ma0121868

19. Parameswaranpillai J, Hameed N, Pionteck J, Woo EM. *Handbook of Epoxy Blends*.; 2017. doi:10.1007/978-3-319-40043-3

20. Garate H, Goyanes S, D'Accorso NB. Controlling nanodomain morphology of epoxy thermosets modified with reactive amine-containing epoxidized poly(styrene-b-isoprene-b-styrene) block copolymer. *Macromolecules*. 2014;47(21):7416-7423. doi:10.1021/ma501496x

21. Balazs AC, Emrick T, Russell TP. Nanoparticle {Polymer} {Composites}: {Where} {Two} {Small} {Worlds} {Meet}. *Science (80-).* 2006;314(5802):1107-1110. doi:10.1126/science.1130557

22. Meng Y, Zhang X. Nanostructured Epoxy Composites. *Micro and Nanostructured Epoxy/Rubber Blends*. 2014;1:53-72. doi:10.1002/9783527666874.ch3

23. Hillmyer MA, Lipic PM, Hajduk DA, Almdal K, Bates FS. Self-assembly and polymerization of epoxy resin-amphiphilic block copolymer nanocomposites. *J Am Chem*

Soc. 1997;119(11):2749-2750. doi:10.1021/ja963622m

24. Blanco M, López M, Kortaberria G, Mondragon I. Nanostructured thermosets from self-assembled amphiphilic block copolymer/epoxy resin mixtures: Effect of copolymer content on nanostructures. *Polym Int*. 2010;59(4):523-528. doi:10.1002/pi.2731

25. Xu Z, Zheng S. Morphology and thermomechanical properties of nanostructured thermosetting blends of epoxy resin and poly(ε-caprolactone)-block-polydimethylsiloxane-block-poly(ε-caprolactone) triblock copolymer. *Polymer (Guildf)*. 2007;48(20):6134-6144. doi:10.1016/j.polymer.2007.07.072

26. Maiez-Tribut S, Pascault JP, Soulé ER, Borrajo J, Williams RJJ. Nanostructured epoxies based on the self-assembly of block copolymers: A new miscible block that can be tailored to different epoxy formulations. *Macromolecules*. 2007;40(4):1268-1273. doi:10.1021/ma062185l

27. Williams RJJ, Rozenberg BA, Pascault J-P. Reaction-induced phase separation in modified thermosetting polymers. 1997:95-156. doi:10.1007/3-540-61218-1_7

28. Meng F, Zheng S, Li H, Liang Q, Liu T. Formation of ordered nanostructures in epoxy thermosets: A mechanism of reaction-induced microphase separation. *Macromolecules*. 2006;39(15):5072-5080. doi:10.1021/ma060004+

29. Fan W, Zheng S. Reaction-induced microphase separation in thermosetting blends of epoxy resin with poly(methyl methacrylate)-block-polystyrene block copolymers: Effect of topologies of block copolymers on morphological structures. *Polymer (Guildf)*. 2008;49(13-14):3157-3167. doi:10.1016/j.polymer.2008.05.010

30. Tamate R, Hashimoto K, Ueki T, Watanabe M. Block copolymer self-assembly in ionic liquids. *Phys Chem Chem Phys*. 2018;20(39):25123-25139. doi:10.1039/c8cp04173c

31. Simone PM, Lodge TP. Lyotropic phase behavior of polybutadiene-poly (ethylene oxide) diblock copolymers in ionic liquids. *Macromolecules*. 2008;41(5):1753-1759. doi:10.1021/ma702252v

32. Bennett TM, Jack KS, Thurecht KJ, Blakey I. Perturbation of the Experimental Phase Diagram of a Diblock Copolymer by Blending with an Ionic Liquid. *Macromolecules*. 2016;49(1):205-214. doi:10.1021/acs.macromol.5b02041

33. Virgili JM, Hoarfrost ML, Segalman RA. Effect of an ionic liquid solvent on the phase behavior of block copolymers. *Macromolecules*. 2010;43(12):5417-5423. doi:10.1021/ma902804e

34. Hoarfrost ML, Segalman RA. Ionic conductivity of nanostructured block copolymer/ionic liquid membranes. *Macromolecules*. 2011;44(13):5281-5288. doi:10.1021/ma200060g

35. Yang G, Song Y, Wang Q, Zhang L, Deng L. Review of ionic liquids containing, polymer/inorganic hybrid electrolytes for lithium metal batteries. *Mater Des*. 2020;190:108563. doi:10.1016/j.matdes.2020.108563

36. Jin M, Zhang Y, Yan C, Fu Y, Guo Y, Ma X. High-Performance Ionic Liquid-Based Gel Polymer Electrolyte Incorporating Anion-Trapping Boron Sites for All-Solid-State Supercapacitor Application. *ACS Appl Mater Interfaces*. 2018;10(46):39570-39580. doi:10.1021/acsami.8b00083

37. Larrañaga M, Martin MD, Gabilondo N, et al. Toward microphase separation in epoxy systems containing PEO-PPO-PEO block copolymers by controlling cure conditions and molar ratios between blocks. *Colloid Polym Sci*. 2006;284(12):1403-1410. doi:10.1007/s00396-006-1512-9

38. Mijovic J, Shen M, Sy JW, Mondragon I. Dynamics and morphology in nanostructured

thermoset network/block copolymer blends during network formation. *Macromolecules*. 2000;33(14):5235-5244. doi:10.1021/ma991894e

39. Guo Q, Thomann R, Gronski W, Thurn-Albrecht T. Phase behavior, crystallization, and hierarchical nanostructures in self-organized thermoset blends of epoxy resin and amphiphilic poly(ethylene oxide)-block-poly(propylene oxide)-block-poly(ethylene oxide) triblock copolymers. *Macromolecules*. 2002;35(8):3133-3144. doi:10.1021/ma011971h
40. Lynd NA, Hillmyer MA. Influence of polydispersity on the self-assembly of diblock copolymers. *Macromolecules*. 2005;38(21):8803-8810. doi:10.1021/ma051025r
41. Huang CI, Lodge TP. Self-consistent calculations of block copolymer solution phase behavior. *Macromolecules*. 1998;31(11):3556-3565. doi:10.1021/ma980007p
42. Hanley KJ, Lodge TP, Huang CI. Phase behavior of a block copolymer in solvents of varying selectivity. *Macromolecules*. 2000;33(16):5918-5931. doi:10.1021/ma000318b
43. Xie S, Meyer DJ, Wang E, Bates FS, Lodge TP. Structure and Properties of Bicontinuous Microemulsions from Salt-Doped Ternary Polymer Blends. *Macromolecules*. 2019;52(24):9693-9702. doi:10.1021/acs.macromol.9b01963

CHAPTER 3: BLOCK COPOLYMER PHASE EVOLUTION VIA REACTION OF THERMOSET RESINS

3.1 Introduction

Previously, it has been discussed that fabricating nanostructured BCP-epoxy composites may be categorized into two strategies: self-assembly, or reaction-induced microphase separation (RIMPS). [1] In self-assembly, the initial BCP-epoxy blend contains self-assembled structures. Those initial structures are preserved or modified throughout the curing process. In RIMPS, the BCP-epoxy blend initially contains no structures, with all components mutually miscible. As the epoxy cures, the BCP becomes less miscible in the matrix. The changing solubility of the block copolymer in the growing epoxy network, coupled with the kinetic trapping that occurs as the molecular weight of the epoxy grows, determines the final structure of the cured material. The final structure is a complex interplay of thermodynamic and kinetic factors – in some cases, it has been shown that modifications in the curing cycle can result in changes in the final cured structure. [2]

In addition, we have shown that ionic liquid acts as an effective selective solvent for a block copolymer. In addition to simply modifying the d-spacing of existing structures, at sufficient concentrations, it induces phase changes and is thus an effective agent for modifying the self-assembly behavior of a triblock copolymer. The specific ionic liquid employed (EMIM-DCA) was chosen for its ability to simultaneously act as a curing agent for the epoxy. In this section, we describe the phase changes that result from curing epoxy present in the ternary blends.

Ionic liquids have a number of potential benefits over traditional curing agents. These include latent curing ability, higher epoxy conversion, flame retardancy, and enhanced

conductivity. [3-9] Additionally, ILs cure the epoxy network through a chain mechanism rather than a step mechanism and thus do not have to be added in strict stoichiometric proportion. [6]

Historically, ionic liquids were first added to epoxy formulations as additives (rather than standalone curing agents) in an effort to improve the processability or add functionality. [10] However, it was eventually shown that some ionic liquids may act as complete curing agents in their own right, with some formulations matching or exceeding the mechanical properties of amine-cured formulations. [3,11] Ionic liquids all share the characteristic of relatively large, charge-dispersed ions (thus their low lattice energy), but there is a wide variety of nucleophilicity and chemistries within the class. Final network properties depend on the nature of the cation as well as the anion, and the exact mechanism by which ionic liquid cures epoxy, especially into a cross-linked network, remains a matter of debate.

The specific ionic liquid used in this work (1-ethyl-3-methylimidazolium dicyanamide, EMIM-DCA, Scheme 2.1) was discovered as an epoxy curing agent fairly recently (2009), [11] and has a few features that make it an attractive curing agent. It is easily incorporated into liquid resins (vs. amines, which are often solid at room temperature and thus be melted first), imparts ionic conductivity to the epoxy network [6], and in some cases may offer increased wear resistance. [8] Its most compelling feature is its latent curing ability; that is, it may be pre-mixed and stored as a stable formulation for months without reacting. [11] A few publications have indicated that the reaction mechanism between EMIM-DCA and epoxide groups is not straightforward, and may involve several simultaneous reactions. [3,12] The dicyanamide ion on its own is capable of the ring-opening epoxide reaction. [5] Under elevated temperatures, the imidazolium cation may also dealkylate (or deprotonate) to form imidazole derivatives, which may initiate a chain polymerization via ring-opening epoxide reactions. [12,13] Regardless of the

specific mechanism, reactions between EMIM-DCA and epoxy proceed rapidly once a threshold temperature is reached. Mechanical properties and T_g of the final epoxy network depend on the initial concentration of EMIM-DCA in the formulation. [5]

In this section, we cure the samples characterized in the previous section utilizing EMIM-DCA as a curing agent. Results indicate that significant phase evolution occurs in nearly all samples. In a few samples, a complex series of order-order transitions occur throughout the curing process. In addition, phase evolution continues even after the curing process is theoretically complete as measured via DSC. The complexity of these change suggests significant future opportunities in engineering materials with a wide variety of possible nanostructures.

3.2 Materials & Methods

Materials

Bisphenol A diglycidyl ether (BADGE), 1-ethyl 3-methyl imidazolium dicyanamide (EMIM-DCA) ionic liquid (IL) (98%), and poly(ethylene oxide-b-propylene oxide-b-ethylene oxide) (PEO20–PPO70–PEO20) (Pluronic, P-123, MW ~5,800 g/mol) were purchased from Sigma-Aldrich and used without further purification.

Blending of Samples

Polymer and IL were added to a mixing cup and heated between 60 and 70 °C until the polymer was fully melted. The sample was then mixed at 2000 rpm for 2 min using a FlakTek SpeedMixer. This mixture was cooled to room temperature after mixing. Subsequently, BADGE was added, and the blend was mixed at 2000 rpm for another 2 min in the SpeedMixer. For small-angle X-ray scattering (SAXS) experiments, the blends were loaded into a 1.5 mm quartz glass capillary using a syringe with a long 22 Ga needle.

Small-Angle X-ray Scattering

SAXS experiments in this section for the in situ cured samples were performed at the Advanced Photon Source at Argonne National Laboratory at beamline 12-BM-B. The average photon energy was 16 keV. Quartz capillaries of the samples were mounted inside a resistance-heated/nitrogen-cooled heating block. The block temperature was ramped to 60 °C and held for 4 h at 60 °C. The temperature was then ramped to 100 °C and held for 4 h before being cooled down to 30 °C. The ramp speed was chosen to reach the set point temperature relatively quickly without overshooting. Set point temperatures were typically reached within 15–20 min during heating steps and 30–40 min during cooling steps. For ex situ curing experiments, samples were cured in the capillaries using a ThermoFisher Heratherm oven. The oven was programmed for an anneal step for 4 h at 60 °C, followed by a cure step for 4 h at 100 °C, and a slow cool down to room temperature (>6 h). Two-dimensional scattering data were collected and azimuthally averaged to generate a 1D plot of scattered intensity versus q, where q is the scattering wave vector. Data was analyzed using custom Matlab scripts.

Dynamic Scanning Calorimetry (DSC)

DSC experiments were performed on a Trios DSC2500 with hermetically sealed aluminum pans. In a typical experiment, samples were subjected to an initial heating cycle from room temperature to 225 °C, cooled to −100 °C, heated to 225 °C, and cooled to room temperature. Experiments were performed at a ramp rate of 10 °C/min.

Rheology

Rheology measurements were performed on a TA Instruments DHR-2 at 1 Hz using a 25 mm parallel plate geometry. Plates were preheated to 100 °C prior to sample loading. Measurements

were performed in stress-controlled mode at 0.5 Pa, and a gap height of 9732 μm. A frequency sweep was first performed to ensure that the sample parameters were within the linear regime.

AFM

Atomic force microscopy (AFM) was performed on an Anton Paar instrument Tosca 400 in tapping mode. Samples were prepared by cracking in half, gluing to a glass slide and using a clean razor blade to shave the exposed surface visually smooth. The tip was coated with aluminum (nominal force constant 40 N/m, resonance frequency 300 kHz, budgetsensors.com).

3.3 Ternary phase diagrams of ionic liquid, block copolymer, and epoxy resin after curing

Data from the previous section (Figure 2.1) show that P-123 BCPs self-assemble into nanostructures in uncured epoxy blends. However, it is well-established that the nanostructures of epoxy/BCP blends may change during epoxy curing. [1,14] To determine whether these changes exist in this system, the samples were subjected to a curing cycle of 4 h at 60 °C, followed by 4 h at 100 °C. After the samples cooled, the structure was determined using SAXS, and a phase diagram of the cured blends was constructed (Figure 3.1). Atomic force microscopy (AFM) was used to verify the disordered micelle structure (Figure 3.6) for the sample designated by the circle in Figure 3.1a. Comparison of Figures 2.1 and 3.1 shows that almost all of the phases evolved significantly. While it was expected that there would be some differences between the two phase diagrams, the observed extent of these changes was surprising.

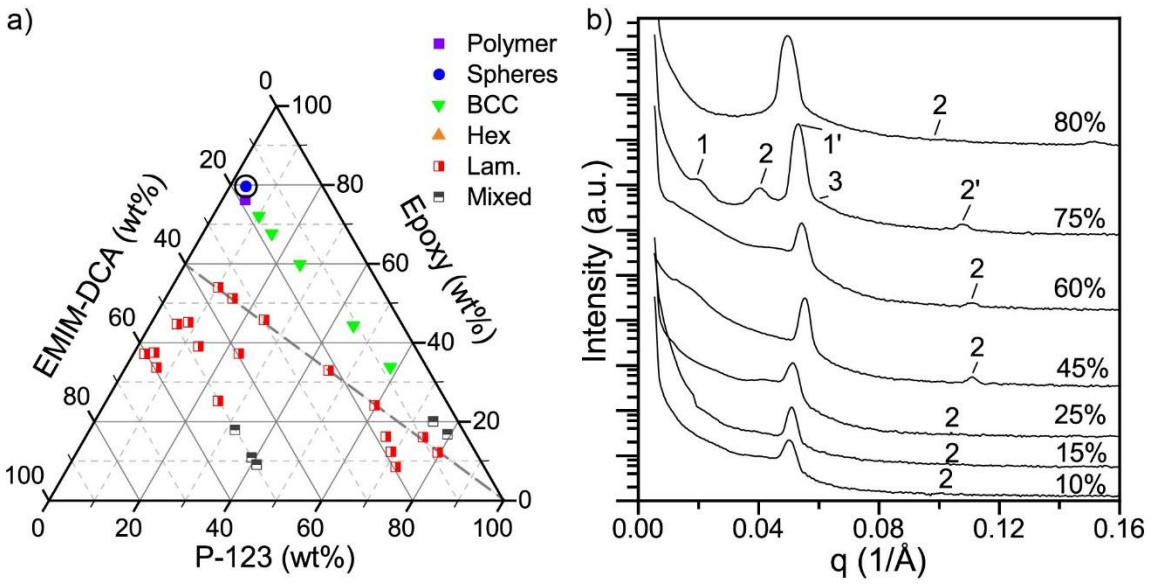

Figure 3.1: *a)* Ternary phase diagram developed for the cured blends of epoxy, EMIM-DCA, and P-123 as determined using SAXS. The grey dashed diagonal line indicates a line of equal ratio epoxy/EMIM-DCA (1.5:1) *b)* Representative SAXS traces are shown for the compositions along the grey dashed line.

The phase evolution of similarly self-assembled BCP-epoxy mixtures upon curing was first described by Lipic et al. [15,16] They describe that as the epoxy network crosslinks, a previously solvated epoxy-soluble chain (here, PEO) is gradually deswelled and locally expelled from the curing network. This “wet-brush” to “dry-brush” transition leads to a change in volume fraction of the epoxy-soluble block at the micelle surface, which results in a change in the interfacial curvature and thus a phase change. Generally, this process results in a relative flattening of the interface, that is, spherical micelles transition to cylindrical micelles, and cylindrical micelles to gyroid or lamellar phases upon epoxy cross-linking. The system described in this work is slightly different, in that the EMIM-DCA and the BADGE are both solvents for the polymers. Hence, while the volume considerations proposed by Lipic et al. are instructive, in this system, the EMIM-DCA is not present in a set stoichiometric ratio to the BADGE. As the polymer is ejected from the curing epoxy network, the IL is distributed in both the PEO and

epoxy phases. Hence, depending on where a composition sits in the phase diagram, the amount of the EMIM-DCA that goes to the epoxy phase or stays with the PEO chains differs.

The described theory by Lipic et al. is consistent for virtually all of the compositions studied in this work, but the extent of the flattening of the interface depends on the region of the phase diagram. The sample either (1) transitioned to a structure with a flatter micellar interface or (2) retained its structure during epoxy curing. In the first case, the disordered spherical micelles were shown to undergo transition to ordered structures in the cured state depending on the initial composition for the mixture. For higher EMIM-DCA concentration, the samples were more likely to undergo transition to lamellar structures upon cross-linking, whereas at lower EMIM-DCA concentrations, BCC phases were formed. In the regions with excess EMIM-DCA, some of the EMIM-DCA is expelled from the epoxy matrix with the PEO, resulting in the lamellar structures that are favored over a wide composition space for the binary EMIM-DCA/P-123 system. When the EMIM-DCA is not in excess, the EMIM-DCA appears to stay with the epoxy phase and the spherical structure is retained and the ordered BCC structure is observed.

In the second scenario, the structures are retained during cross-linking. For example, compositions at low epoxy concentrations, where the initial self-assembled structure was the lamellar phase, the lamellar phases are mostly preserved upon epoxy cross-linking. This result can be explained in that the low overall epoxy content would not result in significant deswelling of the PEO phase. In this case, the epoxy curing process is roughly the equivalent of removing epoxy from the blend, that is, driving it closer to the composition of a binary P-123-IL blend. Also, as can be seen from Figure 3.1, the lamellar phase was predominant for a wide range of P-123/EMIM-DCA composition spaces. To better understand the phase transformation mechanism, a more granular, in situ characterization method was needed.

3.4 In-situ analysis of the curing process

DSC and in situ SAXS were used to monitor the epoxy crosslinking and the BCP phase evolution throughout the curing cycle. DSC of the samples was used to determine the temperature profile to use for in situ SAXS (Figure 3.2). Uncured samples, subjected to a heat-cool-heat cycle, showed a strong exotherm from the epoxy curing during the first heating cycle (Figure 4a). The subsequent heating cycle (after cooling back to 0 °C) reveals no observable exotherm, suggesting that the curing reaction is functionally completed during the first heating scan. To determine whether 100 °C is sufficient to completely cure the epoxy, the uncured samples were held at 100 °C for 4 h to cure the epoxy. After a cool down to 0 °C, the DSC heating cycle was run again and no exotherm was observed, showing that the reaction is essentially complete after 4 h at 100 °C, to the resolution observable by DSC.

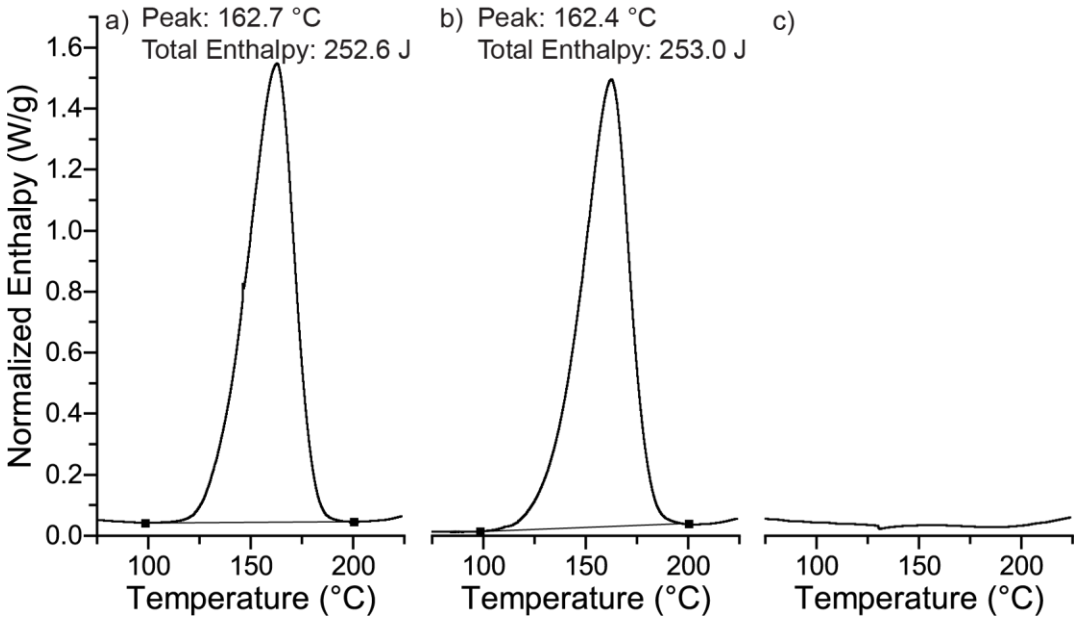

Figure 3.2: *a)* Total exotherm resulting from the curing reaction of an as-prepared sample containing 45 wt % P-123, 33% epoxy and 22% EMIM-DCA. *b)* Exotherm resulting from the curing reaction after being subjected to a 4 h hold at 60 °C. *c)* Exotherm resulting from the curing reaction after being subjected to a 4 h hold at 100 °C.

There was also a desire to identify a moderately elevated temperature, at which the epoxy would not crosslink, to determine whether there was any potential for the BCP to thermally anneal, that is, whether enhanced chain mobility at elevated temperatures would allow the formation of new phases. Samples were held at 60 °C in the DSC for 4 h before the samples were ramped through the epoxy crosslinking temperature. Exotherm analysis was again used to compare the heating cycles, and it was determined that a hold at 60 °C for 4 h resulted in virtually no epoxy crosslinking (Figure 3.2c) Thus, an initial 4 h hold at 60 °C was employed during in situ SAXS experiments to study phase changes due to increased temperature without significant epoxy cross-linking.

One sample (45 wt % P-123, 33% epoxy and 22% EMIM-DCA), at the boundary of the disordered spheres and the ordered phases in the uncured state, was selected for the detailed in situ study. The sample was first exposed to a 4 h hold at 60 °C, a rapid increase to 100 °C, a 4 h hold at 100 °C, and then a gradual drop to room temperature in the SAXS beamline. The SAXS data, collected approximately every 5.75 min, can be seen in Figure 3.3. 2-D line scans at approximately 6, 6.5, 7, and 8 h corresponding to Lam, Gyr, Hex and Dis phases, respectively, are shown in Figure 3.4.

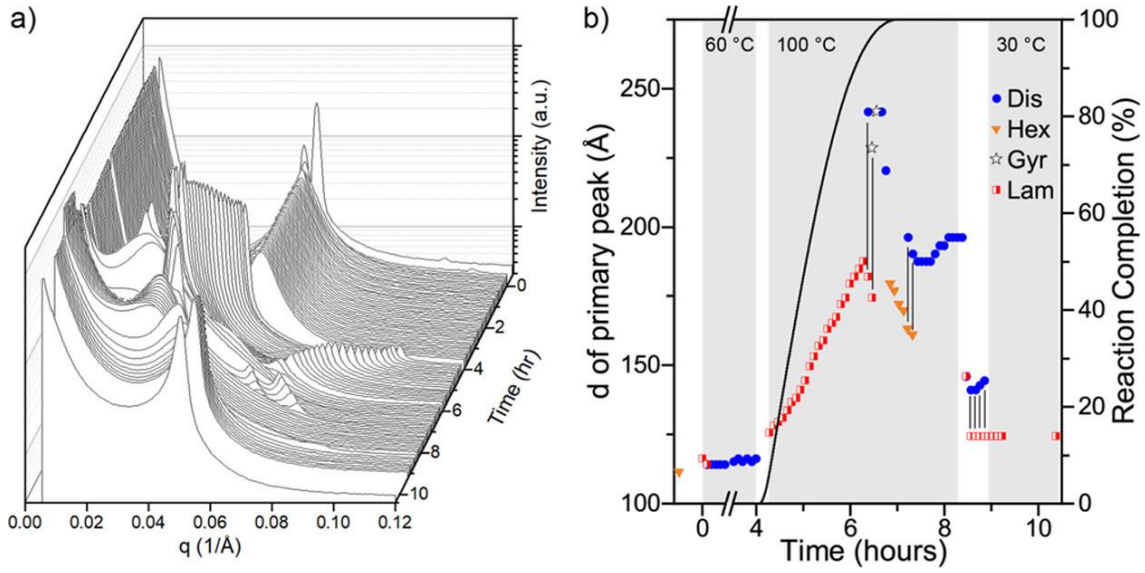

Figure 3.3: a) In situ SAXS profiles taken during the epoxy curing. Sample composition is 45 wt% P-123, 33 wt% epoxy, and 22 wt% EMIM-DCA. The thermal profile consisted of a 4 h hold at 60 °C, a 4 h hold at 100 °C, and a cool down to room temperature. b) BCP phases, and the respective d spacing of the primary peaks, from the in situ SAXS measurements are plotted as a function of time. Samples that showed a coexistence of two phases at one time point are denoted by two data points with a black vertical line between them to indicate the coexistence. The epoxy reaction completion, as determined by DSC, is plotted on the right y-axis.

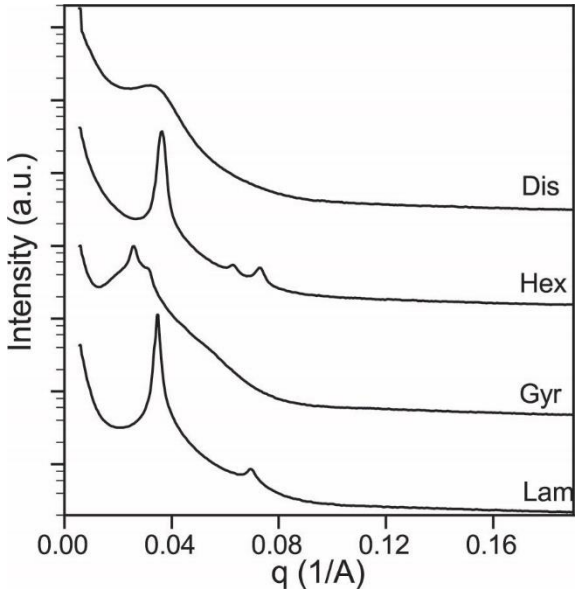

Figure 3.4: Select SAXS linescans from Figure 3.3a, corresponding to representative examples of disordered (Dis), hexagonal (Hex), gyroid (Gyr), and lamellar (Lam) phases.

From these data, it is clear that there were virtually no changes to the structure during the 60 °C hold, but there were complex morphological changes to the blends throughout the 100 °C curing process. To better understand the relationships between the BCP structure and the epoxy cross-linking, the structural information (phase and d spacing) from each SAXS time point can be co-plotted with the extent of epoxy crosslinking from the DSC experiments (Figure 3.3b).

Figure 3.3b reveals that d spacing does not change much within the first 4 hours, but the structure did transition from a Hex/Lam to a disordered structure at the beginning of the hold. The lack of changes in the d spacing indicates that the micelles very likely retain their local ordering, retaining a roughly lamellar shape, but the long-range order is lost due to the elevated temperature and the increased mobility of the polymers. Importantly, the micelles did not become more ordered. It was thus concluded that these phases are not thermally annealed at 60 °C. However, as soon as the temperature is increased above 60 °C (>4 h), there are significant and immediate changes to the d spacing and the structure. The BCPs transition from a disordered structure to a lamellar structure. The d spacing continues to increase until the gyroid structure appears. Initially, there is a coexistence of a disordered phase with the lamellar until the gyroid phase fully appears. This indicates that this disordered phase is likely due to direct transition from the lamellar to the gyroid phase. The gyroid structure has the largest d spacing of any of these structures. At this point (~6.56 h), the sample begins to undergo transition to the Hex structure, through another transition disordered phase, while decreasing the d spacing. Eventually, the structure switches back to the disordered structure with an average d spacing of approximately 19 nm until the sample begins to be cooled back to 30 °C. Finally, once the sample has fully cooled, the lamellar structure stabilizes with a d spacing at approximately 12.4 nm, which is slightly larger than the initial d spacing of 11.6 nm.

Two points stand out from the in situ SAXS data. First, although there were many changes in the structures and domain spacing, there is a strong scattering peak for every time point measured throughout the curing cycle. This indicates that the BCP domains do not fully dissolve in the epoxy at elevated temperatures. In fact, it was observed that the BCP domains appear to go through disordered transition phases as the structures change from one ordered phase to another. While the higher epoxy concentration samples may not show the extent of phase changes as this composition did, virtually all of the samples tested showed some phase change (Compare Figure 2.1 and 3.1). It is likely that the structure in these compositions would also undergo transition through intermediate structures rather than fully dissolving. The second point is that the structural changes continue even when the epoxy cross-linking, as measured by DSC, has completed. Other epoxy/BCP blends have shown that phase transitions continue after the epoxy gel point has been reached but stop before complete epoxy conversion. [14] Here, in some regions of the ternary phase diagrams, including the composition shown in Figure 3.3, large amounts of EMIM-DCA can result in a weak network with a low degree of crosslinking, which may allow for continued phase evolution even after the epoxy curing has completed. To verify this, the rheology of the samples was then measured as a function of the curing reaction at 100 °C (Figure 3.5). The composition described in Figure 5 (45 wt% P-123, 33 wt% epoxy and 22 wt% EMIM-DCA) was cured while taking simultaneous rheological measurements. The parallel plate geometry was pre-heated to 100 °C prior to sample loading. The gel point (i.e. the storage/loss modulus crossover) occurs at approximately 2.5 hours. However, the rheological

data showed that the network continued to stiffen for several hours after reacting the gel point.

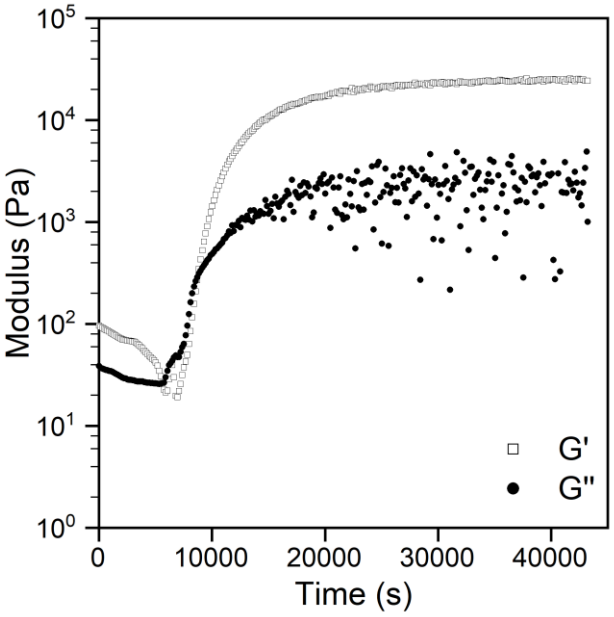

Figure 3.5: Rheological measurements of a sample comprised of 45 wt% P-123, 33 wt% epoxy and 22 wt% EMIN-DCA). The rheometer was prepared with a parallel plate geometry heated to 100 °C.

Interestingly, the DSC data showed that the reaction was nearly complete at 2.5 h, indicating that the epoxy network continued to evolve even after the DSC data showed the reaction had completed. The continued structural evolution of the epoxy network likely resulted in changes to the PEO–epoxy interactions, and thus, it is not surprising that structural changes to the BCP continued to evolve throughout this process. Further study of these systems will be needed to better understand how the phase transitions depend on the ternary compositions and degree of conversion.

A few attempts were made to independently verify the phases identified via SAXS in this work through electron microscopy, but practical elements of sample preparation prevented success. Specifically, samples containing significant amounts of polymer were too soft and sticky to section via conventional microtome methods. However, a successful attempt was made

to characterize a sample via AFM. A sample containing 3.9 wt% P-123, 88 wt% BADGE, and 18.6 wt% EMIM-DCA (corresponding to a disordered spheres phase, circled in Figure 3.1) was characterized, and a representative image is shown in Figure 3.6. High phase (light) and low phase (dark) regions correspond to epoxy matrix and the phase separated PPO domains, respectively. Arrows indicate representative polymer domains.

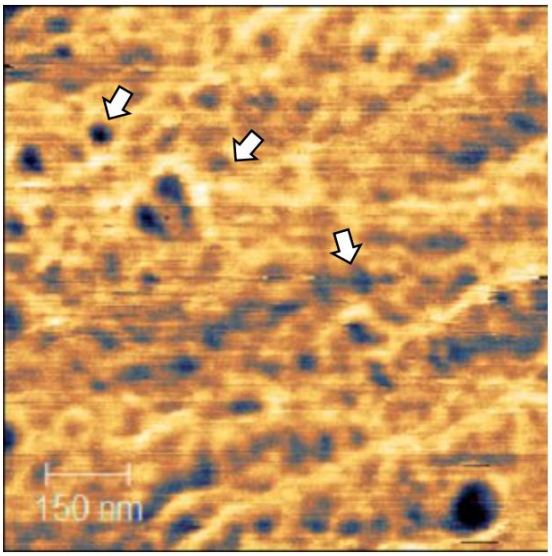

Figure 3.6: AFM image of 3.9 wt% P-123, 88 wt% BADGE, and 18.6 wt% EMIM-DCA cured sample. High phase (light) and low phase (dark) regions correspond to epoxy matrix and the phase separated PPO domains, respectively. Arrows indicate representative polymer domains.

3.5 Conclusion & Future Directions

In this section, we have shown that the complex phase behavior exhibited by the ternary blends of block copolymer, ionic liquid, and epoxy evolve significantly when the epoxy is cured. Although the phase changes may be somewhat rationalized with arguments about polymer solubility and mobility, the complexity of these phase changes – and the continued evolution of phase after the experimental heating was complete – points to future opportunities in engineering materials with a wide variety of possible nanostructures.

The curing cycle in this work was chosen to impart maximum mobility to the block copolymer and epoxy throughout the curing cycle. It has previously demonstrated that the curing cycle can dramatically alter the nanostructure of an epoxy composite (and its subsequent properties). [17] Future work may evaluate the effect of curing cycle on the final material structure in formulations of this type. For instance, does an extended hold at 100 °C yield a different material nanostructure than (say) 150 °C? Evaluation of these effects may lead to the development of materials with switchable properties, depending on the desired application, from a single formulation. In addition, elevated cure temperatures may alter the progression of the epoxy cure cycle and change the mechanical properties of the epoxy matrix.

Our work has also demonstrated that ionic liquids significantly alter the nanoscale structure of polymer epoxy composites, and opportunities exist in modifying the formulation to take advantage this feature while improving the properties of the epoxy. We have demonstrated that complex phase behavior exists in certain regions of the ternary phase diagram, but some of those regions are subject to excessive plasticization from excess ionic liquid or polymer. It is also unclear to what degree an epoxy network is formed when ionic liquid is added in excess. Both rheological experiments and qualitative evaluations of the cured material reveal that in the case of materials with high polymer or ionic liquid content, the final material is of relatively low modulus. It is unclear if this is because the mechanical properties are dominated by the relatively soft polymer, or if the epoxy network is insufficiently crosslinked to form a high-modulus network. Future work may seek to decouple the structure-directing properties of the ionic liquid from its curing ability, and thus preserve the robust mechanical properties of the epoxy with the complex nanostructure and functionality offered by ionic liquid-modified block copolymer

fillers. This may be accomplished by employing non-curing ionic liquids, or blending in amounts of more traditional curing agents alongside the ionic liquid.

Portions of this text are modified from previously published work.

Liu, D & Krogstad, D. V. Self-Assembly and Phase Transformation of Block Copolymer Nanostructures in Ionic-Liquid Cured Epoxy. Macromolecules 2021, 54, 2, 988–994. doi.org/10.1021/acs.macromol.0c02214

References

1. Jose S, George SM. Handbook of Epoxy Blends. *Handb Epoxy Blends*. 2015. doi:10.1007/978-3-319-18158-5
2. Romeo HE, Zucchi IA, Rico M, Hoppe CE, Williams RJJ. From spherical micelles to hexagonally packed cylinders: The cure cycle determines nanostructures generated in block copolymer/epoxy blends. *Macromolecules*. 2013;46(12):4854-4861. doi:10.1021/ma400778s
3. Maka H, Spychaj T, Pilawka R. Epoxy resin/ionic liquid systems: The influence of imidazolium cation size and anion type on reactivity and thermomechanical properties. *Ind Eng Chem Res*. 2012;51(14):5197-5206. doi:10.1021/ie202321j
4. Silva AA, Livi S, Netto DB, Soares BG, Duchet J, Gérard JF. New epoxy systems based on ionic liquid. *Polymer (Guildf)*. 2013;54(8):2123-2129. doi:10.1016/j.polymer.2013.02.021
5. Maka H, Spychaj T, Zenker M. High performance epoxy composites cured with ionic liquids. *J Ind Eng Chem*. 2015;31:192-198. doi:10.1016/j.jiec.2015.06.023

6. Maksym P, Tarnacka M, Dzienia A, et al. Enhanced Polymerization Rate and Conductivity of Ionic Liquid-Based Epoxy Resin. *Macromolecules*. 2017;50(8):3262-3272. doi:10.1021/acs.macromol.6b02749

7. Livi S, Duchet-Rumeau J, Gérard JF, Pham TN. Polymers and ionic liquids: A successful wedding. *Macromol Chem Phys*. 2015;216(4):359-368. doi:10.1002/macp.201400425

8. Jiang Z, Wang Q, Liu L, Zhang Y, Du F, Pang A. Dual-Functionalized Imidazolium Ionic Liquids as Curing Agents for Epoxy Resins. *Ind Eng Chem Res*. 2020;59(7):3024-3034. doi:10.1021/acs.iecr.9b06574

9. Carvalho APA, Santos DF, Soares BG. Epoxy/imidazolium-based ionic liquid systems: The effect of the hardener on the curing behavior, thermal stability, and microwave absorbing properties. *J Appl Polym Sci*. 2020;137(5):1-11. doi:10.1002/app.48326

10. Tamate R, Hashimoto K, Ueki T, Watanabe M. Block copolymer self-assembly in ionic liquids. *Phys Chem Chem Phys*. 2018;20(39):25123-25139. doi:10.1039/c8cp04173c

11. Hanze AR, Conger TW, Wise EC, Weisblat DI. Room Temperature Ionic Liquids as Thermally Latent Initiators for Polymerization of Epoxy Resins. *Macromolecules*. 2009;42(9):3219-3221. doi:10.1021/ja01211a087

12. Binks FC, Cavalli G, Henningsen M, Howlin BJ, Hamerton I. Investigating the mechanism through which ionic liquids initiate the polymerisation of epoxy resins. *Polymer (Guildf)*. 2018;139:163-176. doi:10.1016/j.polymer.2018.01.087

13. Farkas A, Strohm PF. Imidazole catalysis in the curing of epoxy resins. *J Appl Polym Sci*. 1968;12(1):159-168. doi:10.1002/app.1968.070120115

14. Blanco M, López M, Kortaberria G, Mondragon I. Nanostructured thermosets from self-assembled amphiphilic block copolymer/epoxy resin mixtures: Effect of copolymer

content on nanostructures. *Polym Int*. 2010;59(4):523-528. doi:10.1002/pi.2731

15. Lipic PM, Bates FS, Hillmyer MA. Nanonstructured thermosets from self-assembled amphiphilic block copolymer/epoxy resin mixtures. *J Am Chem Soc*. 1998;120(35):8963-8970. doi:10.1021/ja981544s

16. Hillmyer MA, Lipic PM, Hajduk DA, Almdal K, Bates FS. Self-assembly and polymerization of epoxy resin-amphiphilic block copolymer nanocomposites. *J Am Chem Soc*. 1997;119(11):2749-2750. doi:10.1021/ja963622m

17. Romeo HE, Zucchi IA, Rico M, Hoppe CE, Williams RJJ. From spherical micelles to hexagonally packed cylinders: The cure cycle determines nanostructures generated in block copolymer/epoxy blends. *Macromolecules*. 2013;46(12):4854-4861. doi:10.1021/ma400778s

CHAPTER 4: THERMAL DECOMPOSITION OF ACYLGLYCEROLS AND THEIR CORROSIVE EFFECT ON CARBON STEEL

4.1 Introduction

Acylglycerols are a broad class of molecules comprised of fatty acids attached to a glycerol molecule through an ester linkage (Scheme 4.1). Acylglycerols and their derivatives (e.g. monoglycerides and fatty acids) are ubiquitous in biological molecules and thus essential building blocks for living organisms.

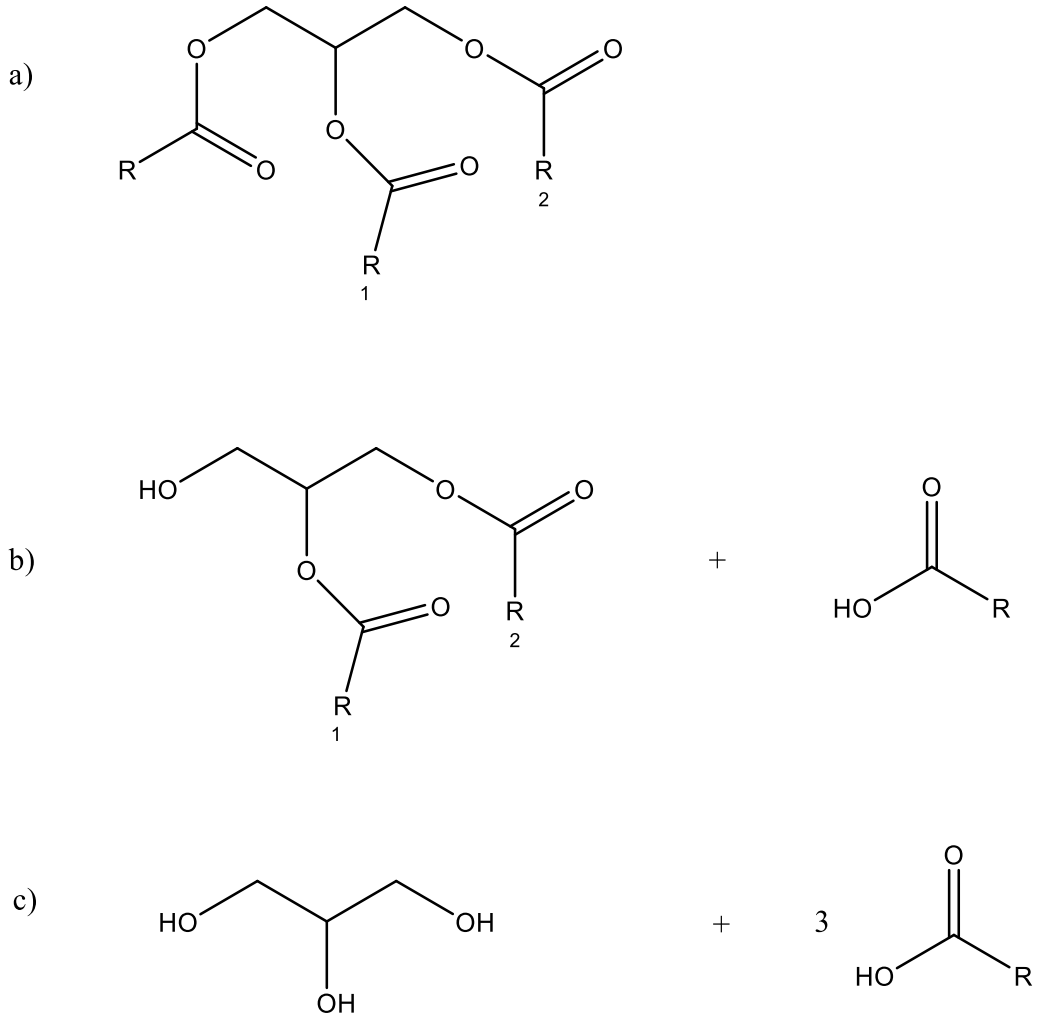

Scheme 4.1: Typical acylglycerol species. *a)* intact triglyceride, with R-groups representing carbon tails with various lengths and numbers of double bonds *b)* Triglyceride partially decomposed into diglyceride, with associated free fatty acid *c)* Triglyceride broken down into glycerol and three fatty acids

In addition to their importance to the natural world, the wide availability and low cost of acylglycerols makes them important as commercial feedstocks. Acylglycerols feature heavily in a wide variety of consumer (including personal care and food), industrial, and agricultural products. [1] In the past few decades, an increasing share of the acylglycerol market has been consumed by the energy sector. [2] Early attempts to divest the domestic energy economy of the United States from foreign oil sources led to interest in fuel formulations containing molecules that could be produced domestically, i.e. derived from agricultural products. [3] Interest in this work has not waned since then. Current US consumption of biofuels has eclipsed 15 billion gallons annually. [2] As a stable global petroleum supply becomes increasingly untenable for reasons of both geopolitical stability and environmental sustainability, relatively mature technologies are being called upon to fill the gap until second-generation biofuels e.g. lignocellulose or biomass-derived fuels may be brought online. [4]

The oleochemical process pathway [4], which directly refines acylglycerol-based oil and fats into fuels, comprises a relatively small share of the biofuel market but nonetheless is of significant technological importance. A crucial advantage of acylglycerol feedstocks (over e.g. processed intermediates) is that they may be directly co-refined with petroleum, i.e. they may be directly swapped for petroleum in existing processes without the substantial capital investment of new processing equipment. [5,6] When coupled with the wide availability of acylglycerol feedstocks and the well-established supply chain, the oleochemical process pathway is among the most cost-effective methods for refiners to incorporate feedstocks of biological origin (or ‘biofeedstocks’) into their portfolio.

One key shortcoming of acylglycerol feedstocks, and a feature that limits their broader adoption, is their increased reactivity and reduced stability as compared to petroleum.

Acylglycerol feedstocks have substantially different chemistry than traditional petroleum feedstocks- namely, they contain a large number of oxygen-containing moieties including esters, carboxylic acids, and alcohols. These chemical differences result in a feedstock with higher reactivity, lower thermal stability, and increased hydrophilicity than a petroleum feedstock. [5] Acylglycerols are particularly troubling for their corrosivity towards the metallurgies used in process units. The corrosive capability of a feedstock is measured via its total acid number, defined as the mg of kOH required to neutralize the acids present in 1 gram of sample. [7] An unblended acylglycerol biofeedstock has a wide range of possible acid numbers (e.g. 2-3 for purified soybean oil to ~80 for pyrolysis oil), but the total acid number is generally far above the industry standard of 0.5 for petroleum feedstocks. [5]

Current accepted best practice for using biofeedstocks is either conservative blending with existing petroleum feedstocks or installing dedicated process units with upgraded metallurgy. [5] However, these practices limit the processable volume of the biofeedstocks with existing infrastructure and thus the commercial and environmental benefit of switching. There is thus substantial interest in an improved understanding of the mechanisms that lead to biofeedstock-induced corrosion, as well as methods to reduce the corrosivity of a particular feed. This would enable processors to increase biofeedstock volume while minimizing the potential for corrosion-caused equipment failure.

In this section, we perform systematic experiments to understand the chemical changes occurring in a variety of biofeedstocks as they are subjected to elevated temperatures and pressures, typical of refining processes. Biofeedstocks were held in contact with carbon steel coupons to evaluate their corrosive behavior, and changes in the feedstock and the steel surface were evaluated throughout the early stages of the corrosion process (0-30 hours). Although a

huge variety of chemical reactions are possible and we do not rigorously prove that certain reactions are occurring, we identify a few trends that inform an overall picture of the chemical environment as reactions progress.

Food-grade triglyceride oils (e.g. soybean, palm, or tallow) consist predominantly of mostly intact triglyceride, with only trace amounts of free fatty acid and phospholipids. [8] We show that triglycerides readily break down into mono- and di- glyceride species, releasing free fatty acid (likely through nucleophilic attack at the ester bond). Secondary reactions of the fatty acid occur at later stages of the reaction, releasing water into the biofeedstock. These experiments inform the following section, wherein we perform experiments characterizing reverse micelle-forming acylglycerol mixtures in white oil. By exploiting the amphiphilic nature of monoglycerides, we demonstrate that reverse micelles can be formed by appropriate mixtures of monoglycerides in white mineral oil, and that fatty acids and polar solvents may be incorporated into solution while keeping the micelle intact. We hope to lay the groundwork for the design of biofeedstock mixtures that neutralize corrosive species by designing mixtures that sequester the more corrosive (i.e. more polar) species.

4.2 Materials & Methods

Materials

The acylgycerols used in this work are food grade soybean oil, palm oil, and tallow. They were mixed with white mineral oil in various compositions to mimic an industrial biofeedstock formulation. Carbon steel 1018 coupons were used for corrosion experiments. All preceding materials were obtained from BP. A few experiments utilize purified versions of species found in acylglycerol solutions. Triolein, lauric aldehyde, heptadecanone, decanoic, oleic acid, and stearic acid were obtained from Sigma-Aldrich and used as received.

Sample Preparation

Acylgycerol solutions (termed 'biofeedstock' in the rest of this work) were prepared by weighing an appropriate amount of acylglycerol and mineral oil into a glass vial, and then mixing vigorously on a stirplate for at least 10 minutes. Palm oil and tallow containing solutions were heated to above their melting point while mixing. Samples are named in the format (feedstock)(##)(solvent), where feedstock represents the acylglycerol (S=soybean oil, Pa= palm oil, T= tallow), the two numbers represent the weight percent of the acylglycerol , and solvent represents the balance of the solution (W=white oil). Thus, S10W represents a 10 wt% soybean oil, 90 wt% mineral oil solution. Carbon steel 1018 (CS1018) metallic coupons, 5 mm X 5 mm X 0.5 mm, were machined by electrical discharge machining (EDM) and polished with 320 grit silicon carbide paper.

Autoclave process

A 316 stainless steel autoclave manufactured by Park Hannifin (model 60 ml EZE Seal Pressure Vessel) was used for the experiments. The autoclave is rated to 78 bar at 274 °C. Prior to corrosion testing, the CS1018 coupons were polished using 320 grit SiC paper, sonicated in isopropyl alcohol for several minutes and rinsed with additional isopropyl alcohol. Then, they were mounted in a sample holder of the same alloy as the autoclave, configured with three slits over a deeper groove [9], and submerged in 10 mL of prepared biofeedstock solution before being air-sealed in the autoclave. A standard experiment included three coupons. The autoclave was then placed in a Mellen Microtherm 1200 °C box furnace. The furnace was heated to 274 °C at 10 °C/min and held for the specified experimental time. The autoclave was subsequently allowed to cool inside the furnace until safe to handle (about 14 hours). Biofeedstock solution and coupons were then removed for characterization. For all experiments, prior to

characterization the coupons were removed from the autoclave, rinsed with toluene and sonicated for 5 minutes in toluene. This process removed loosely adhered species from the surface.

TGA

TGA was performed on a Q50 from TA instruments, under a flow of dry air and a ramp rate of 20 °C/min.

FTIR

Attenuated total reflectance – Fourier transform infrared spectroscopy (ATR-FTIR) was performed on a Bruker Alpha II with Platinum-ATR module. Liquid sample was placed on the ATR, fully covering the diamond ATR crystal. The IR spectra was measured from 4000 to 400 cm^{-1} with a total of 64 scans and a resolution of 4 cm^{-1}. FTIR peaks were fit via the peak-fitting function in Origin Pro 2020 to identify individual peak areas.

Karl-Fischer Titration

Water content was measured via coulometric Karl Fischer Titration, using a Metrohm 917 Coulometer equipped with a Metrohm 885 autosampler oven. Water vapor was extracted from the samples at a furnace temperature of 120 °C under a constant flow of dry air at 50 mL/min and directed into the reaction vessel.

Corrosion Experiments

The carbon steel coupons were weighed before and after the autoclave process using a XPE26 microbalance from Mettler-Toledo. The corrosion rate was determined by measuring the net mass loss from the cleaned coupon after the autoclave experiments were completed. Uniform corrosion rates in mils per year (mpy) are calculated from the coupon mass loss through $MPY =$

$\frac{534\,W}{DAT}$, where W is mass loss in milligrams, D is density in grams per cubic centimeter, A is the area in square inches, and T is time in hours

4.3 FTIR and thermal analysis of various acylglycerol solutions

To determine the preferred autoclave temperature, TGA experiments were performed to show the thermal decomposition of the biofeedstocks and their components under dry air (Figure 4.1). Results shows that the white oil is substantially more volatile than the soybean oil. The autoclave temperature of 274 °C was chosen where mass loss of the soybean oil was in its early stages, but white oil had not yet totally decomposed.

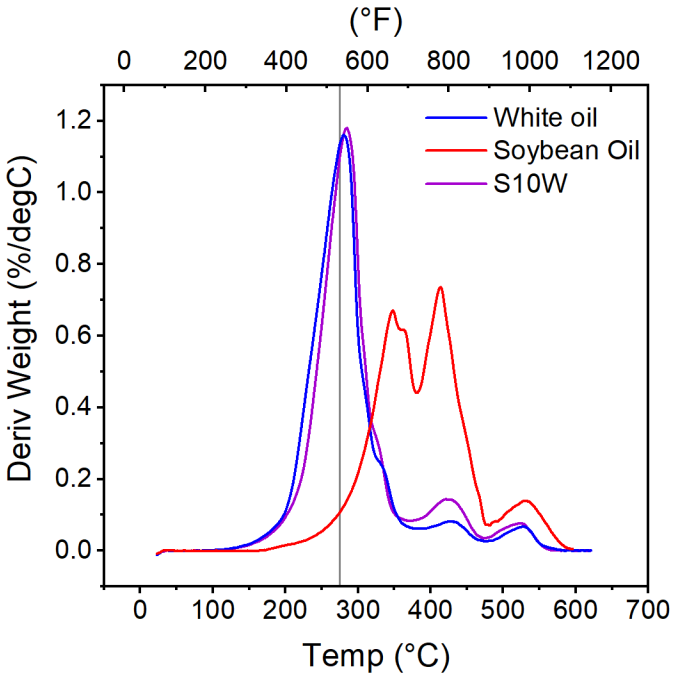

Figure 4.1: TGA of a 10 wt% soybean oil mixture, and the pure components.

In the initial experiments, a 10 wt% soybean oil solution (S10W) was sealed in an autoclave with 3 carbon steel coupons and was held at 274 °C. A series of experiments at various hold times was performed. ATR-FTIR spectroscopy was used to identify chemical species evolution in the biofeedstock (Figure 4.2). In these data, a few key regions reveal systematic

changes in the peak intensity as a function of autoclave time. The peak at ~1740 cm^{-1}, highlighted in Figure 4.2b, decreases with increasing autoclave time. This peak is assigned to the stretch mode of the carbonyl bond in an ester [10], which in the current system corresponds to the esters that attach the fatty acids to the glycerol in the TAG. There is also a systematic decrease in the peaks between 1050 and 1250 cm^{-1}. These peaks correspond to the stretch of the alkyl- and acyl- C-O bonds [10], which may be associated with ester carbon-oxygen bonds in the present system. The final peak with significant change is at ~1715 cm^{-1}. This peak is initially not present, but is present by 1 hour and increases in height through 10 hours (Figure 4.2b). The peak remains approximately constant between 10 and 20 hours but decreases by 30 hours. This peak corresponds to the carbonyl stretch of a non-ester bond, e.g. a carboxylic acid, a ketone or an aldehyde. [11]

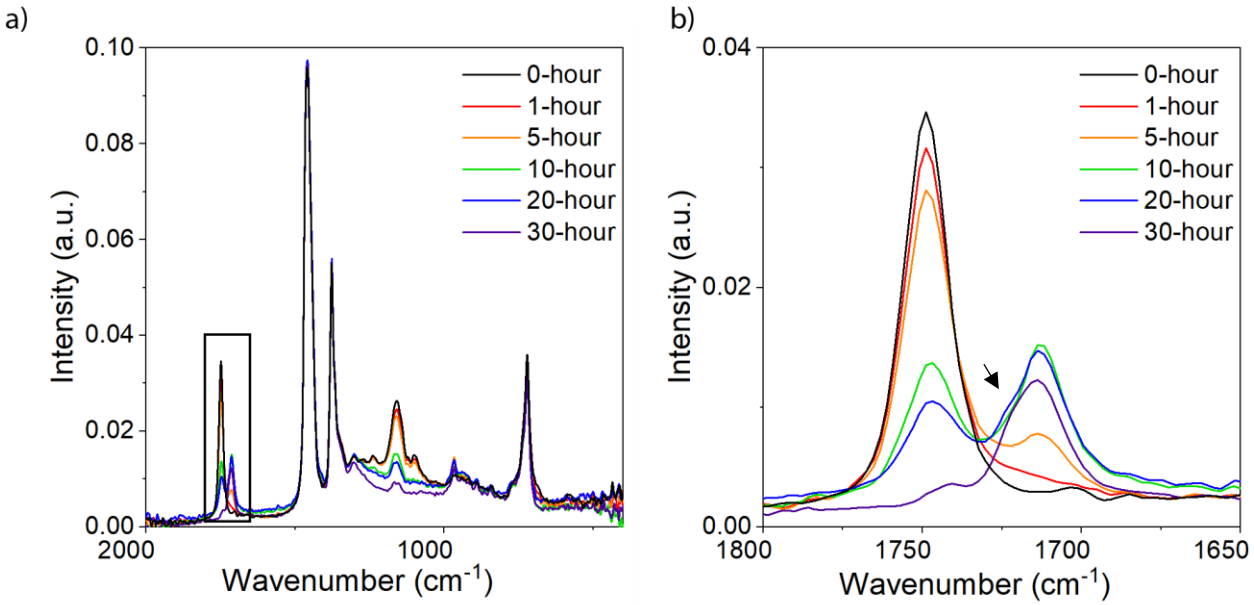

Figure 4.2: *a)* Representative FTIR of S10W samples at various timepoints. *b)* Detailed view of the 1650-1800 cm^{-1} region, showing systematic decrease of the ester carbonyl peak corresponding to glycerol-attached species, and corresponding growth of free carbonyl-type species (carboxylic acids, ketones, aldehydes). The arrow corresponds to the growth of species from secondary reactions after the 10-hour mark.

To verify that the peaks corresponded to the species we identified, as well as confirm that the relationship between bond concentration and peak area was a linear relationship, ATR-FTIR was performed on commercially acquired representative species of the two bond types. For the 'attached' ester bond, a commercial triolein was characterized. For the 'free' bond, various fatty acids, lauric aldehyde (representing aldehydes) and heptadecanone (representing ketones) were characterized. Location of the peak maximum in each case corresponded to our peak assignment in the FTIR. It was found that fatty acids are centered around the primary peak location at ~1715 cm^{-1} location, while ketones and aldehydes correspond to the location of the shoulder appearing at the 10-hour mark. In addition, it was found that the intensity peak was linear with concentration across the experimental concentration range for 'attached' species (Figure 4.3a). For the 'free' species, the relationship was linear but varied in slope for species type (Figure 4.3b)

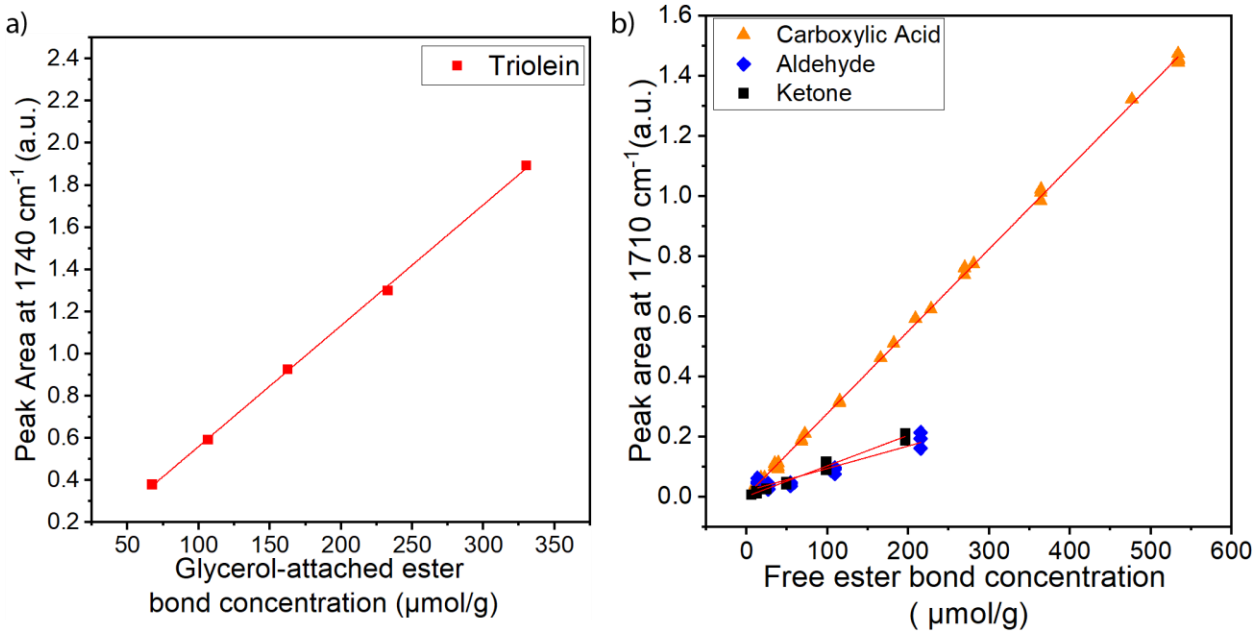

Figure 4.3: Calibration curves of concentration vs. peak area at various locations. *a)* Glycerol-attached ester bonds, as represented by a model triglyceride (triolein) *b)* Free ester bonds, with various species. Ketones are represented by heptadecanone and aldehydes by lauric aldehyde. Carboxylic acid is a mixture of decanoic, oleic, and stearic acid.

The convoluted peaks in Figure 4.2 were fit with Origin Pro 2020, using a Pseudo-Voigt function. Since we had previously established that concentration and total peak area have a linear relationship, the area of the peak at 1740 cm^{-1} may be directly correlated to concentration. Thus, the FTIR data shows that the glycerol-attached ester concentration decreases with increasing autoclave time until the esters are virtually gone by 30 hours (Figure 4.4). Non-ester carbonyls (e.g. aldehydes, carboxylic acids or ketones) do not have a consistent slope for the relationship between peak area and species concentration, and thus the area of the peak centered around ~1710 cm^{-1} cannot be strictly correlated to concentration (Figure 4.3b). However, it is apparent that the peak increases in area for the first 10 hours, then plateaus and decreases through 30 hours. This change in area is more easily visualized if peak areas are plotted as a function of time, shown in Figure 4.4 This analysis was repeated for a 25 wt% solution of soybean oil, S25W, and both S10W and S25W are shown. The steady decrease in total peak area indicates that either species concentration in solution is decreasing (through e.g. sorption to surrounding surfaces or transfer to the gas phase) or some species are converting to other species with weaker signal intensity in FTIR (e.g. carboxylic acids to ketones or aldehydes).

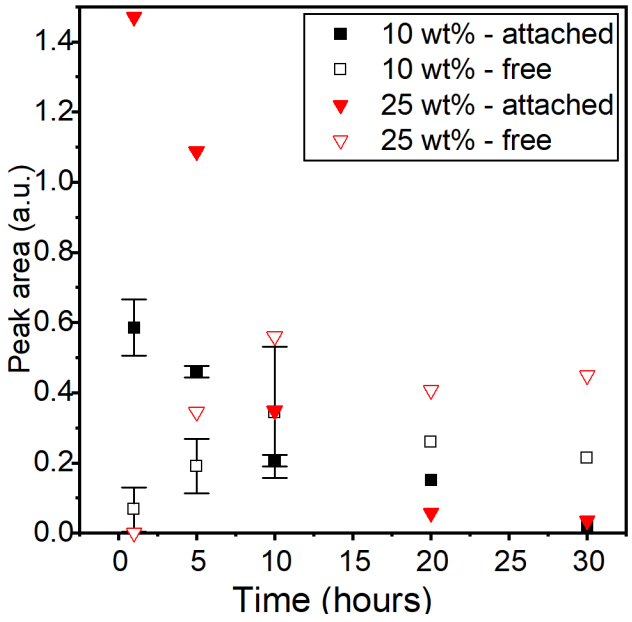

Figure 4.4: Peak areas in FTIR for soybean oil, centered around 1740 cm-1 (attached) and 1710 cm-1 (free) as a function of time in the autoclave.

It is apparent from Figure 4.4 that the triglycerides present in the soybean oil readily break down under the conditions of the autoclave, with signal intensity from free species peaking at 10 hours for both S10W and S25W. Signal intensity for attached species disappears almost entirely by the 30-hour mark, indicating nearly complete breakdown of glycerol-attached species.

Other aldehyde biofeedstocks (palm and tallow oil) were analyzed in an identical fashion (Figure 4.5). Solutions of 10 wt% palm oil and tallow were prepared as described in the methods section. Although there is significant uncertainty in the data, the general trend of a plateau in free species by 10 hours, with almost no intensity from attached species by 30 hours, is preserved.

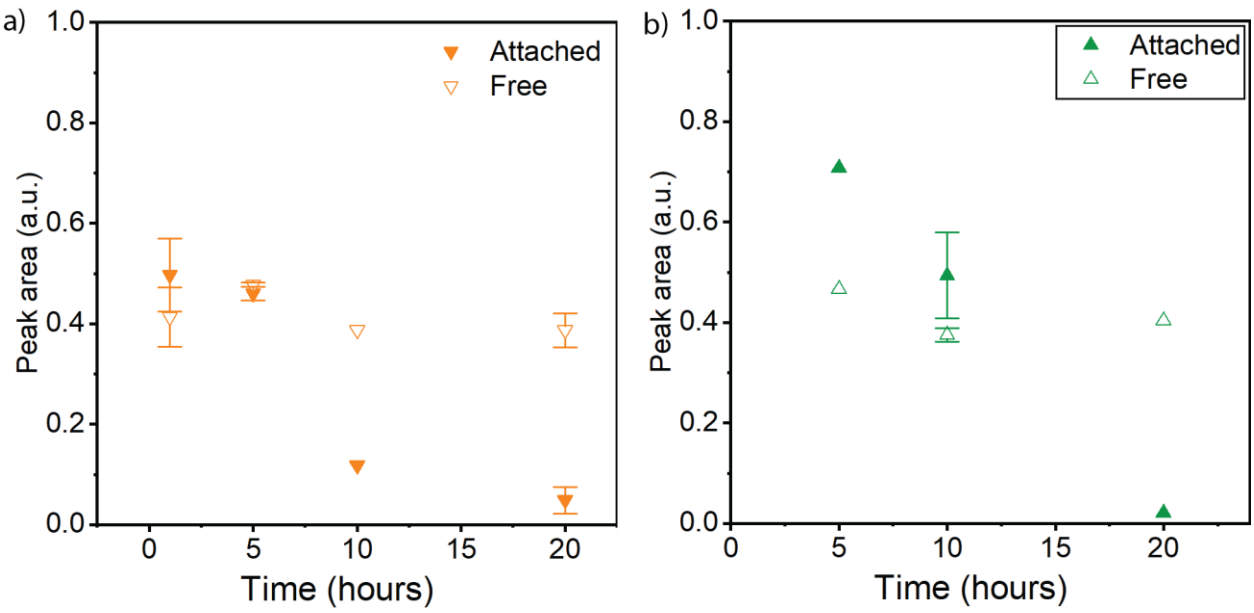

Figure 4.5: Peak areas in FTIR for for the two peaks centered around 1740 cm-1 (attached) and 1710 cm-1 (free) as a function of time in the autoclave for *a)* palm oil and *b)* tallow oil

4.4 Corrosion of carbon steel coupons

Results of the previous section demonstrated that triglycerides break down readily in the autoclave process. Results are shown in Figure 4.7a for corrosion from the carbon steel coupons sealed in the autoclave with the biofeedstock. Measurable corrosion is observed at the 5-hour mark. The corrosion rate peaks at 10 hours and then reduces until the 30-hour mark. Although the rate of corrosion decreases after 10 hours, total corrosion continues to increase.

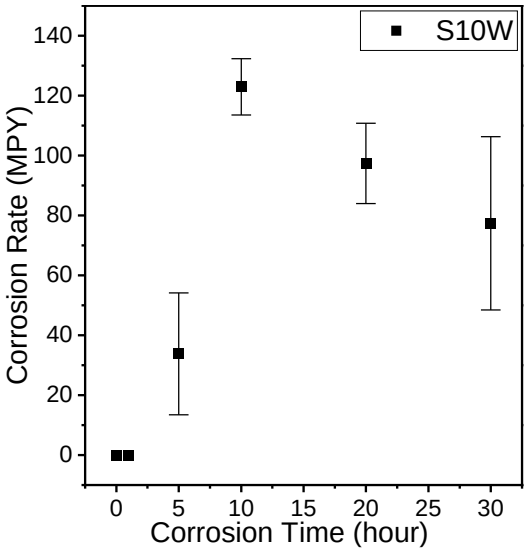

Figure 4.6: Corrosion of carbon steel coupons autoclaved with S10W biofeedstock solution, expressed as a corrosion rate. Corrosion rate peaks at 10 hours and slows through 30 hours, though total corrosion continues to increase.

4.5 The effect of the metal coupon

Since corrosion is the result of reactions between the metal coupon and the feedstock, it was expected that the presence of the coupon should have an effect on the reactions occurring in the biofeedstock. To probe the effect of reducing the number of carbon steel coupons (and thus the available surface area for any reactions between biofeedstock and carbon steel), a few experiments were performed with modified metal coupons. Results are shown in Figure 4.7 for FTIR analysis (as in Section 4.3) performed on S10W autoclaved with no coupon, or a stainless steel coupon. Significantly more attached ester remains in the absence of carbon steel, showing that the presence of the carbon steel accelerates the breakdown of the acylglycerol.

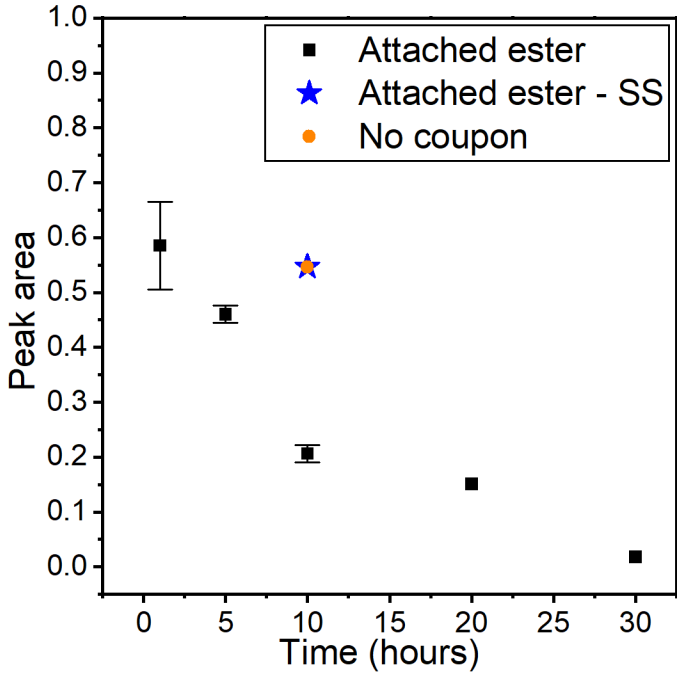

Figure 4.7: Peak area from FTIR analysis of an autoclaved S10W solution, reporting the peak centered around ~1740 cm-1 and corresponding to an attached ester bond. Results from a solution with no carbon steel coupons, or stainless steel coupons, show significantly more intact ester bonds at the 10-hour timepoint.

To further explore this effect, a series of experiments varying the amount of carbon steel coupon (1 or 3) present in the autoclave. Since less carbon steel is present in the 1-coupon case, it was expected that the rate of acylglycerol breakdown be reduced vs. the 3-coupon case. Both a 10 wt% biofeedstock and a 25 wt% biofeedstock were tested. Results from the FTIR analysis are shown in Figure 4.8. By 20 hours, although the amount of remaining triglyceride is nearly identical, there are significantly more free species than in the 3-coupon case.

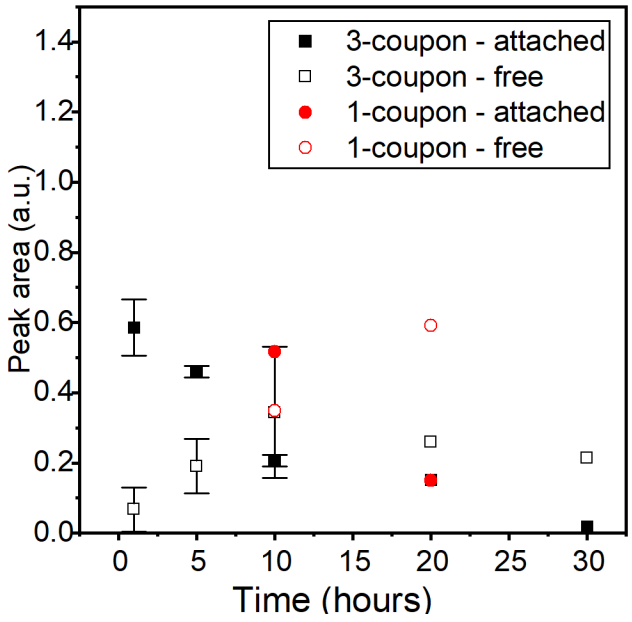

Figure 4.8: Peak area from FTIR analysis of an autoclaved S10W (filled) and S25W (open) solution. Attached corresponds to a glycerol-attached ester bond, and free to a free ester bond (corresponding to a fatty acid, aldehyde, or ketone). Data with 1 carbon steel coupon contains more fatty acid than the 3-coupon case at 20 hours of autoclave time.

The preceding results showed that more breakdown of the biofeedstock occurred in the presence of iron steel than in the absence. Since iron ions are capable of catalyzing or otherwise participating in many organic reactions [12], we were interested in the effect of simply dissolving iron ions in solution. To probe this effect, a biofeedstock was prepared with dissolved iron stearate and run for 10 hours in the autoclave. No carbon steel coupon was included, as the effect of just the dissolved ion was of interest. FTIR (Figure 4.9) show that the FTIR spectra most closely resembled that of an autoclave experiment with no coupon, implying that iron ions dissolved in solution alone is insufficient for accelerating triglyceride breakdown.

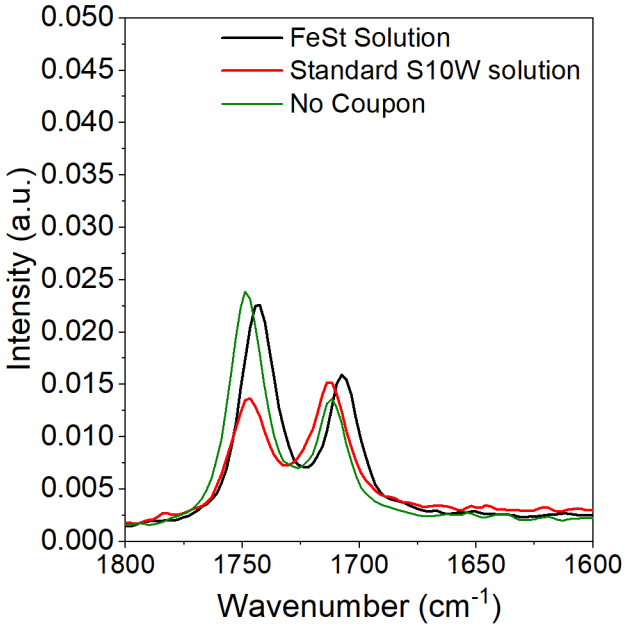

Figure 4.9: Detailed FTIR of an S10W solution with iron stearate (FeSt) solution autoclaved with no carbon steel coupon, vs. a standard S10W solution autoclaved with no coupon or 3 coupons (standard). FeSt solution more closely resembles the no coupon case.

Together, Figures 4.7-4.9 suggest that carbon steel – and specifically the carbon steel surface – participates in the reactions of the acylglycerol. In the total absence of carbon steel (i.e. with a stainless steel coupon, or no coupon) the acylglycerol remains more intact at the 10-hour mark. This is not the case if iron ions are simply dissolved in the biofeedstock solution. With only limited amounts of carbon steel present, the extent of acylglycerol breakdown is within the error bar at 10 hours. However, at 20 hours, more fatty acid remains in solution in the 1-coupon case. This implies that carbon steel is also important for the secondary reactions of the fatty acid, discussed in the following section.

4.6 The effect and generation of water

Since the most likely reaction of the acylglycerol in the autoclave is hydrolysis, the evolution of water was tracked throughout the autoclave process via Karl Fischer (KF) coulometric analysis. It was determined that neat soybean oil has a water content of 239.0 ± 25.5

ppm (5 measurements) and white oil has a water content of 11.9 ± 0.5 ppm (3 measurements). Unexpectedly, the water content of S10W solutions increases with autoclave time (Figure 4.10) throughout the process.

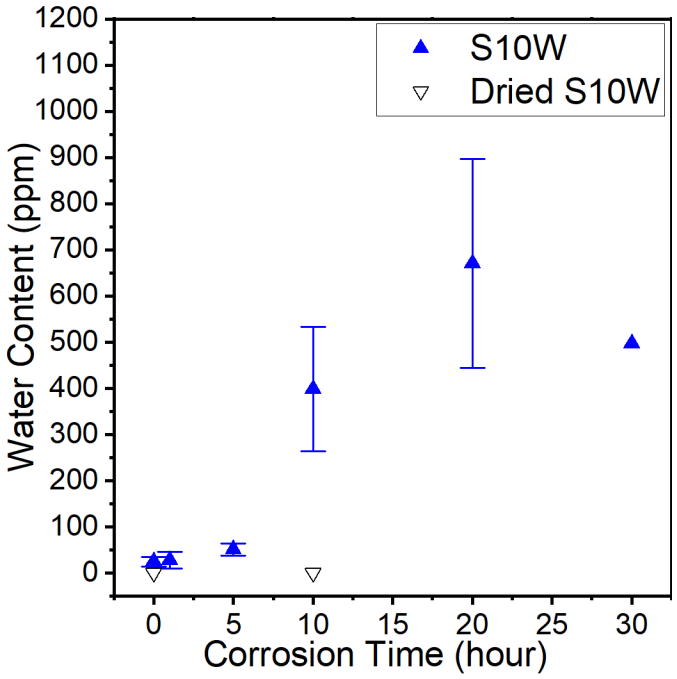

Figure 4.10: Water content of an S10W solution, measured via Karl-Fischer coulometric titration after the autoclave process. Water content is initially within the limits of resolution of the instrument, but grows significantly between hours 5 and 10. A dried S10W solution shows less water at both the 1-hour and 5-hour timepoints compared to an unmodified solution.

This increase in water content is surprising, as the presumed primary method of water consumption – acylglycerol hydrolysis – is occurring rapidly between hours 5 and 10. Water may be plausibly generated through a few mechanisms, as shown in Scheme 4.2. First, free glycerol can dehydrate in an acidic environment to generate water and various ketone species. [14] Second, free carboxylic acids may undergo ketonization, generating water and carbon dioxide. Ketonization is known to be accelerated by the presence of certain metal oxides [15] including iron oxide. [16,17] Additionally, the ATR-FTIR data in Figure 2b shows the

development of a shoulder at 1720 cm^{-1}, which could be associated with the formation of ketone molecules from two free fatty acids. Lastly, free fatty acids can react with a basic surface of iron oxide on the coupon surface, releasing water.[18] They may also physiosorb, which does not generate water. [19] Interestingly, the reactions of fatty acid with the carbon steel surface also help explain the data shown in Figure 4.8, where a reduced amount of carbon steel results in more free fatty acids in solution. It is important to note that this is an extremely limited selection of reactions among the many that could be occurring in the autoclave and the potential impact of pressure on the proposed reactions has not been explored. However, the proposed subset of reactions do proceed readily at the experimental temperature (274 °C) and are consistent with the experimental observations in this work. More studies will be needed to elucidate which water-generating reactions are the most prominent in these systems.

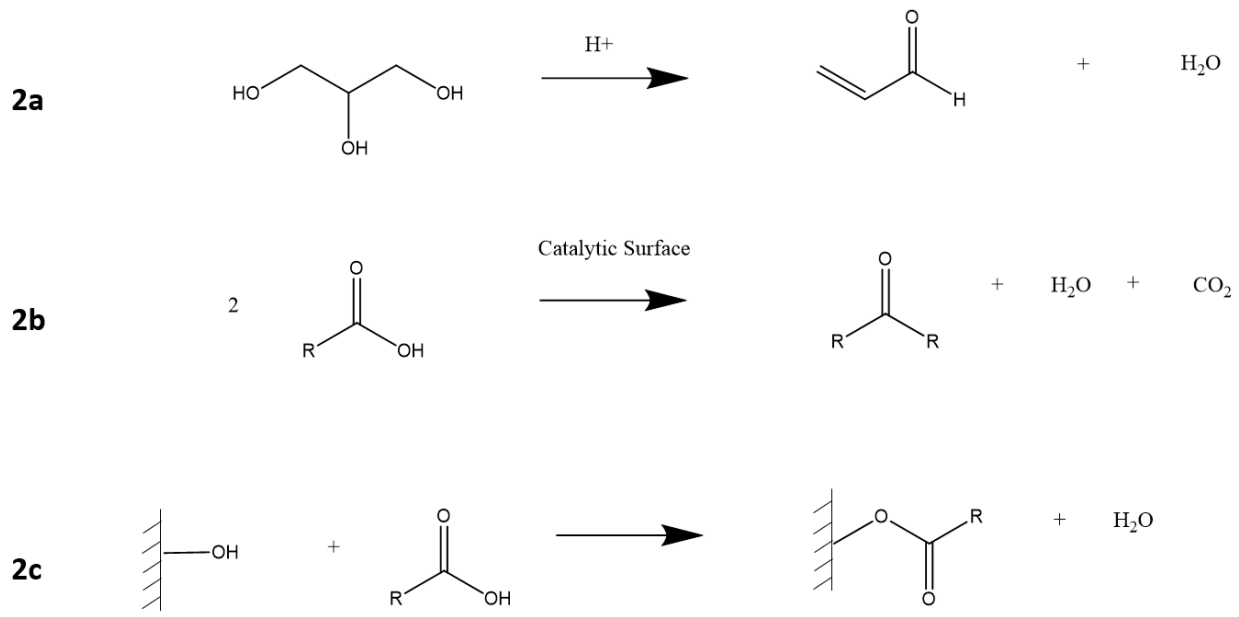

Scheme 4.2: Possible water-generating reactions that may be occurring in the biofeedstock throughout the autoclave process. *a)* dehydration of glycerol in an acidic environment *b)* ketonization of fatty acids *c)* condendsation reaction between free hydroxyls on the iron surface and a fatty acid

One natural question is whether the biofeedstock is simply absorbing water from the atmosphere after it was removed from the autoclave. Since the biofeedstock solution post-autoclave is expected to be more hydrophilic than the solution as-prepared, care was taken to characterize solutions promptly (within an hour) after removal from the autoclave. Interestingly, measuring the same sample over time (Figure 4.11) revealed that water content in the feedstock solutions actually dropped over time rather than rising, as it would if the decomposed biofeedstock were absorbing water from the environment (Samples were stored in tightly sealed vials, but under atmospheric conditions.)

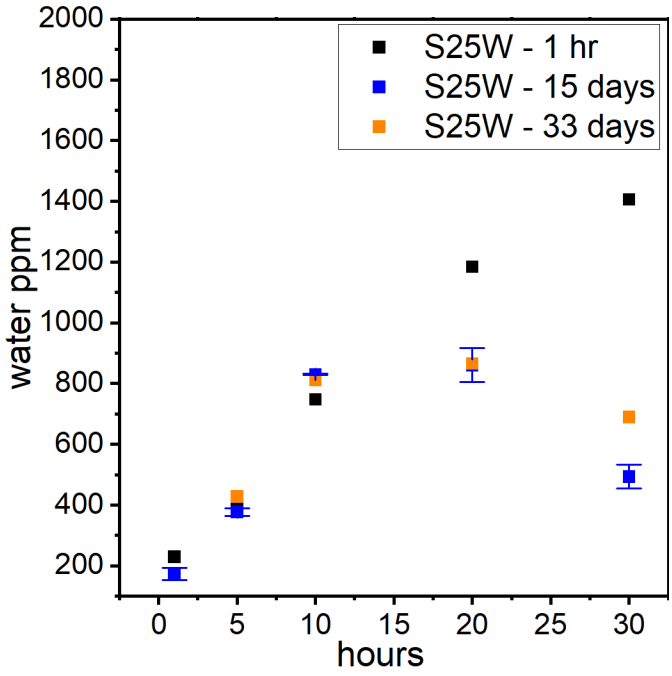

Figure 4.11: KF titration of the same solution over a period of many days. S25W was removed from the autoclave and measured for water content repeatedly. Subsequent KF measurements show that water content in solution actually drops over time.

Since water is an essential participant in the hydrolysis reaction, it was hypothesized that a dry S10W solution would undergo less thermal breakdown. To that end, one experiment was performed where water was removed from the biofeedstock. To remove water from the

feedstock, S10W was sealed in a round bottom flask and nitrogen was bubbled through the biofeedstock overnight. Water content was confirmed to be functionally zero, within the limits of detection of the KF instrument. The dried biofeedstock was then quickly transferred to the autoclave and a normal 10-hour autoclave experiment was performed. FTIR analysis (Figure 4.12) also showed that significantly more triglyceride was broken down in the dried solution vs. the unmodified solution. This is the opposite of what was expected, as a basic understanding of the hydrolysis reaction indicates the presence of water should promote triglyceride breakdown into fatty acids, and the absence of water should prevent this reaction.

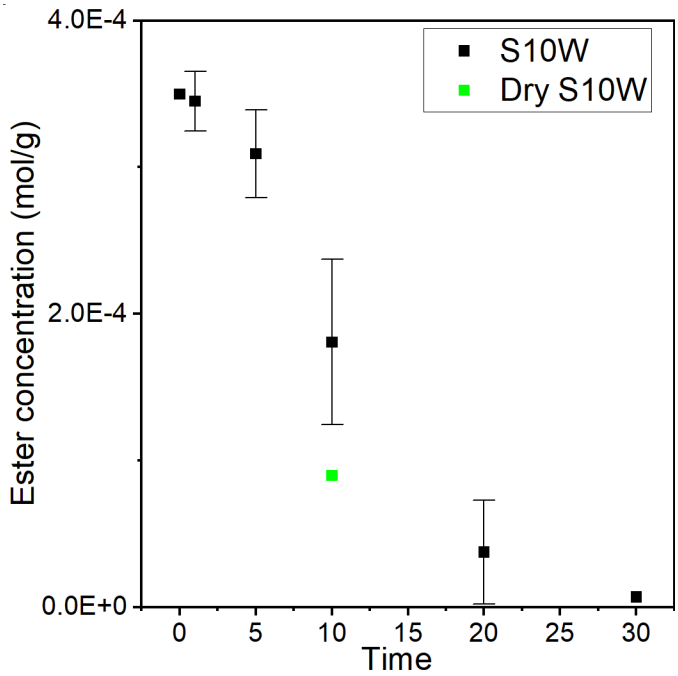

Figure 4.12: FTIR analysis of a dried S10W solution, compared to an unmodified S10W. Significantly less ester remains at the 10-hour mark in the case of the dried solution.

Interestingly, water content in the dried biofeedstock after the autoclave was much drier than in the case of the unmodified feedstock (Figure 4.10). Although it is not clear why this would be the case, it is apparent that the triglyceride breakdown reaction proceeds readily even

in the absence of free water in solution. A brief calculation reveals that the water present in the headspace of the autoclave (10 μmol based on the 10 mL headspace, 50% humidity and 25 °C air), plus water initially measured in the biofeedstocks (~11 μmol), is insufficient to hydrolyze the present triglycerides to the degree that was observed via FTIR (460 μmol is needed to hydrolyze the triglycerides to the extent observed at 10 hours). It is likely that there is a water-generating reaction occurring during the autoclave process that accounts for the concomitant triglyceride hydrolysis and increase in the water content of solution. This becomes more apparent when considering that the water content of the solution actually increases after 5 hours, when it should be consumed in acylglycerol hydrolysis.

4.7 Conclusion & Outlook

Corrosion of carbon steel by triacylglycerol-based feeds can be understood as a complex process wherein bulk solution reactions affect surface reactions and vice versa. Whereas a traditional understanding of corrosion attributes the corrosivity of a feed to a single feature (the acid content), our results show a complex reaction space suggesting many opportunities for corrosion mitigation. Similarly, the chemical changes in the biofeedstocks solution throughout the autoclave process suggest that strategies for neutralizing corrosive species (or preventing their formation altogether) will differ at different points in the process. Prior to 10 hours, the data is consistent with straightforward hydrolysis of triacylglycerols and corrosion due to the increased acidity of the resulting fatty acids. Following 10 hours, the emergence of additional species in FTIR and an increase in water content suggests that secondary reactions become dominant.

Significant opportunity remains in this space to more precisely identify the reactions that are occurring in the biofeedstock throughout the autoclave process. Although our work has

shown the metal coupon is significantly interacting with the biofeedstock throughout the autoclave process, the details of the reactions occurring between the coupon and the biofeedstock are unknown. Experiments with direct detection methods, e.g. GC-MS may provide direct evidence of which species are generated in the autoclave reactions. In addition, we have not identified reactions occurring among the alkyl tails of the fatty acids (which are expected to be significant) or conditions which lead to the formation of physical or chemical gels (i.e. polymerization). Though we made a qualitative observation that the stored biofeedstock thickened over time and in some cases gelated, no attempt to quantify or characterize this aging process was made. Further work is needed to identify whether these structures may serve to protect the steel surface. In addition, our results with water removed from solution (Figures 4.10 and 4.12) show that reaction effects between the carbon steel surface and free water in solution are not trivial. More experimental work is required to replicate and verify this effect.

The objective of the work in this section was twofold. First, we sought to perform a systematic study identifying key reactions and factors that are important during the corrosion of industrially important metals by biofeedstock solutions. To that end, systematic corrosion studies were performed on carbon steel coupons exposed to a biofeedstock comprised of various acylglycerol oils and fats in white oil. Both coupon and biofeedstock were sealed together in an autoclave at 274 °C and the chemical and morphological evolution was characterized over the first 30 hours. Identifying these key reactions and processes informed the second objective, which was to identify opportunities for mitigating corrosion that build on processes that are already occurring during the corrosion reaction. In the following section, we employ natural amphiphiles that are formed as triglycerides break down (i.e. monoglycerides), along with water (which we identified as a prominent reactant of interest in this section), to formulate micelle-

forming biofeedstock solutions. Our preliminary work shows that reverse micelles are readily formed by monoglyceride species, and that the features of these reverse micelles are modifiable with the addition of water or fatty acid.

4.8 References & Acknowledgements

Portions of this work were performed by collaborators. Corrosion data was collected and analyzed by Soheil Daryadel and Samyukta Shrivastav. The author gratefully acknowledges the assistance of Nathan Levandovsky for assistance with FTIR data collection and analysis.

Portions of this text are modified from a manuscript in preparation for publication.
Liu, D., Shrivastav, S., Daryadel, S., Levandovsky, N., An, H., Chen, Q., Krogstad, DV, Krogstad, J. Reactions Between Carbon Steel and Triacylglycerol-based solution at Elevated Temperature.

1. Tyson KS, Bozell J, Wallace R, Petersen E, Moens L. Biomass Oil Analysis : Research Needs and Recommendations Biomass Oil Analysis : Research Needs and Recommendations. *Contract*. 2004;(June):116. http://oai.dtic.mil/oai/oai?verb=getRecord&metadataPrefix=html&identifier=ADA435922.
2. Administration USEI. *March 2022 Monthly Energy Review* . Vol 0035.; 2022.
3. D. D. Songstad, P. Lakshmanan, J. Chen, W. Gibbons SH and RN. Historical Perspective of Biofuels: Learning from the Past to Rediscover the Future. *Vitr CellDevBio*.

2009;45(27):189-192. doi:10.1007/s 11627-009-9218-6

4. Huber GW, Iborra S, Corma A. Synthesis of transportation fuels from biomass: Chemistry, catalysts, and engineering. *Chem Rev*. 2006;106(9):4044-4098. doi:10.1021/cr068360d

5. Marker T. *Opportunites for Biorenewables in Oil Refineries*. Vol DE-FG36-05.; 2005.

6. van Dyk S, Su J, Mcmillan JD, Saddler J (John). Potential synergies of drop-in biofuel production with further co-processing at oil refineries. *Biofuels, Bioprod Biorefining*. 2019;13(3):760-775. doi:10.1002/bbb.1974

7. ASTM. *American Society of Testing and Materials: Annual Book of Standards*.; 2019. doi: 10.1520/D0664-18E02.

8. Dijkstra AJ. Soybean Oil. *Encycl Food Heal*. 2015:58-63. doi:10.1016/B978-0-12-384947-2.00638-3

9. Shetty PP, Daryadel S, Haire BT, et al. Low-Temperature Pack Aluminization Process on Pipeline Steel to Inhibit Asphaltene Deposition. *ACS Appl Mater Interfaces*. 2019;11(50):47596-47605. doi:10.1021/acsami.9b17430

10. Lin-Vien D, Colthup NB, Fateley WG, Grasselli JG. Compounds Containing the Carbonyl Group. *Handb Infrared Raman Charact Freq Org Mol*. 1991;3:117-154. doi:10.1016/b978-0-08-057116-4.50015-8

11. Arslan FN, Caglar F. Attenuated Total Reflectance–Fourier Transform Infrared (ATR–FTIR) Spectroscopy Combined with Chemometrics for Rapid Determination of Cold-Pressed Wheat Germ Oil Adulteration. *Food Anal Methods*. 2019;12:355-370.

12. Fürstner A. Iron catalysis in organic synthesis: A critical assessment of what it takes to make this base metal a multitasking champion. *ACS Cent Sci*. 2016;2(11):778-789.

doi:10.1021/acscentsci.6b00272

13. *Psychrometric Charts*.; 2001. doi:10.1175/1520-0493(1938)66<178:pc>2.0.co;2

14. Rosas IP, Contreras JL, Salmones J, et al. Catalytic dehydration of glycerol to acrolein over a catalyst of Pd/LaY zeolite and comparison with the chemical equilibrium. *Catalysts*. 2017;7(3):1-29. doi:10.3390/catal7030073

15. Pham TN, Sooknoi T, Crossley SP, Resasco DE. Ketonization of carboxylic acids: Mechanisms, catalysts, and implications for biomass conversion. *ACS Catal*. 2013;3(11):2456-2473. doi:10.1021/cs400501h

16. Kuriacose JC, Jewur SS. Studies on the surface interaction of acetic acid on iron oxide. *J Catal*. 1977;50(2):330-341. doi:10.1016/0021-9517(77)90042-2

17. Bennett JA, Parlett CMA, Isaacs MA, et al. Acetic Acid Ketonization over Fe3O4/SiO2 for Pyrolysis Bio-Oil Upgrading. *ChemCatChem*. 2017;9(9):1648-1654. doi:10.1002/cctc.201601269

18. Huang YC, Fowkes FM, Lloyd TB. Acidic and basic nature of ferric oxide surfaces. Adsorption, adhesion, zeta potentials and dispersibility in magnetic inks for hard disks. *J Adhes Sci Technol*. 1991;5(1):39-56. doi:10.1163/156856191X00819

19. Hackerman N, Cook EL. Adsorption of polar organic compounds on steel. *J Phys Chem*. 1951;55(4):549-557.

CHAPTER 5: REVERSE MICELLES OF ACYLGLYCEROL AMPHIPHILES IN NONPOLAR ALKYL ENVIRONMENTS

5.1 Introduction

In the previous section, the major reactions occurring in a acylglycerol-based biofeedstock at elevated temperature were described. The triglycerides present in a food-grade oil readily decompose under the elevated temperature and pressure of the autoclave setup, and fatty acids are not significantly consumed by secondary reactions until after the 10-hour mark. Thus, there is a window of reaction time where the biofeedstock solution is comprised of the relatively more polar triglyceride breakdown products in a solvent of long-chain alkyl species (white mineral oil). The intermediate breakdown products of the triglyceride are amphiphilic, with the exposed alcohol headgroups of the glycerol acting as the hydrophilic portion and the carbon tail the hydrophobic.

In this section, we will discuss efforts to characterize reverse micelles of monoglycerides in white oil. Using species that are triglyceride breakdown products, and thus likely to be present in actual processing conditions, we design micelle-forming formulations at compositions approximating processing conditions for biofeedstocks. The objective of this work was to identify conditions necessary for reverse micelles to exist in biofeedstock mixtures, and explore how those conditions changed with added water or fatty acid. By identifying these conditions, we hope to inform the future design of biofeedstock mixtures that are less corrosive than their TAN or water content would suggest. If polar and reactive species may be sequestered within reverse micelles, they are unavailable for reaction with their surroundings and thus neutralized as corrosive agents. By utilizing an amphiphile already present in a biofeedstock, we inform the design of blends that do not require new considerations for process chemistry.

5.2 Thermodynamics of Reverse Micelles

Reverse micelles are the analogue of normal phase micelles in non-polar solvents, where the polar head group of an amphiphile is directed towards the core rather than the corona. One key difference in the thermodynamic balance of reverse micelles is the absence of the solvophobic/hydrophobic effect. In normal phase micelles, nonpolar species in the vicinity of water cause the water molecules to spontaneously rearrange in a structured fashion, causing a decrease in entropy and thus an unfavorable increase in free energy. [1]Thus, the strong tendency to minimize contact between nonpolar species and water leads to the formation of micelles. This effect is reduced greatly in reverse micelle systems. [2,3] The interaction of a nonpolar surfactant tail with another tail is thermodynamically equivalent (or nearly equivalent) to an interaction with the nonpolar solvent. Thus, the main driving force of micellization is the enthalpic interactions between the polar headgroups of the surfactant. Since there is less thermodynamic cost to a polar head group interaction with nonpolar solvent (versus a nonpolar tail with an aqueous solvent, as in normal phase micelles), the cost of shielding the micelle core with a large micelle is offset by the loss of entropy in organizing a large number of surfactant molecules. Thus, reverse micelles are generally smaller than normal phase micelles. [1]

There is some debate on the use of ‘micelle’ to describe what some argue should instead be called microemulsions or aggregates. Normal-phase micelles are characterized by a step change in properties (e.g. surface tension, optical properties) [4] in the solution at the onset of micellization. In some cases, reverse micelles are observed to form at a critical concentration or temperature in the same manner as normal phase micelles. [5,6] However, in other cases there is instead a gradual increase in the observed aggregation number. [7-9] In the following sections, we describe our observations of x-ray scattering consistent with aggregates gradually

disappearing with rising temperature. This suggest that our observed aggregates are slowly dissolving rather than suddenly crossing a thermodynamic threshold. (They form in a similar manner upon gradual cooling below the dissolution temperature). We refer to these aggregates as micelles, following the convention of a few other authors in recent years. [5,7,10-12]

5.3 Reverse Micelles of Monoglycerides

The monoglycerides used in this work, glycerol monooleate (GMO) and glycerol monostearate (GMS), are typical of monoglycerides found in triglyceride mixtures of soybean oil. The moderate amphiphilicity of monoglycerides and their biocompatibility makes them useful as emulsifiers in a variety of food and consumer product applications. Fatty acids are also frequently incorporated into these emulsions as co-surfactants to tune the material properties (e.g. viscosity). [8]

A few existing pieces of work have explored the phase boundaries of monoglyceride reverse micelles. Shrestha, et al. found that swapping the nonpolar solvent from hexane to hexadecane induced changes in the shape of a GMO micelle. [10] Additional work with a variety of monoglycerides found that aggregation numbers rose with increased polar solvent or decreased temperature. [7,11,13] However, this is the first work systematically characterizing the phase changes over wide composition and temperature ranges for these molecules. In addition, we have utilized a nonpolar, non-volatile oil as a solvent, a significant deviation from the use of volatile organic solvents reported in previous works.

5.4 Materials & Methods

Materials

1-oleyol glycerol at >95% purity was the only isomer of glycerol monooleate (GMO) used in this work. GMO was sourced from Sigma-Aldrich and Cayman Chemical and used interchangeably as-received. Glycerol monostearate (GMS) is a mixture of isomers, with varying attachment points of the fatty acids onto the glycerol. GMS was sourced from Fisher-Scientific and used as received. White mineral oil was obtained from BP and used as received. Oleic acid was sourced from Sigma-Aldrich and used as received.

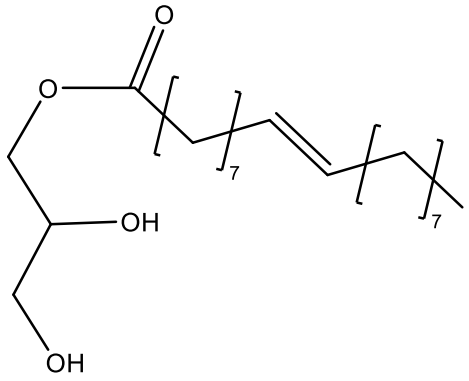

Glycerol monooleate

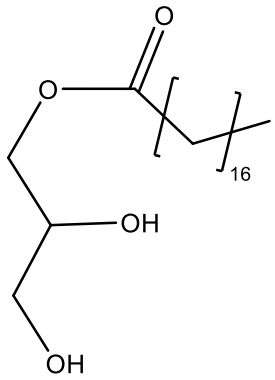

Glycerol monostearate

Scheme 5.1: The two monoglycerides used in this work. Glycerol monooleate (GMO) is an oleic acid with one unsaturated bond attached to a glycerol headgroup, and glycerol monostearate (GMS) is a completely saturated stearic acid attached to the glycerol headgroup.

Sample Preparation

Monoglyceride and white oil were placed in a vial and heated on a stir plate at about 60 °C until melted. The sample was stirred during heating. Additional materials (e.g. water, glycerol, or fatty acid) were then added and the sample was stirred briefly over heat until the sample appeared homogeneous. Samples were then loaded into quartz capillaries using a syringe fitted with a long 22Ga needle.

Small-Angle X-ray Scattering

SAXS experiments were performed at the Advanced Photon Source at Argonne National Laboratory at beamline 12-ID-C. Quartz capillaries of the samples were mounted inside a resistance-heated/nitrogen-cooled heating block. In a few cases, the sample block window was covered with Kapton film.

Data was processed and integrated to 1-D linescans with custom Matlab scripts written by beamline staff of Sector 12 at the Argonne APS. Fitting of the experimental data to a Guinier-Porod model was performed with Irena, a custom Igor program written by Jan Illavsky. [14]

5.5 Phase Diagrams of Binary Monoglyceride-White Oil Mixtures

In initial experiments, monoglyceride was blended with white oil to determine the minimum concentration for the onset of micellization (or critical micelle concentration, CMC). The temperature was then raised until any features observed in SAXS had disappeared and the scattering resembled that of featureless solvent scattering. A series of 1-D traces without background subtraction and arbitrarily scaled for clarity is shown in Figure 1 at selected points along the temperature ramp. Crystallization is observed at low temperatures below the melting point of the pure monoglyceride. The diffraction peaks are observed in a ratio for lamellar phase, which is typical for crystallized monoglycerides [15] (these phases are designated ‘structure’ in

the following figures). Above the melting temperature, a feature is observed which resembles a partial Bessel oscillation typical of pure form factor scattering (30 °C), which we attribute to reverse micelle features. This feature weakens in intensity (60 °C), as the temperature is raised, and eventually disappears (90 °C).

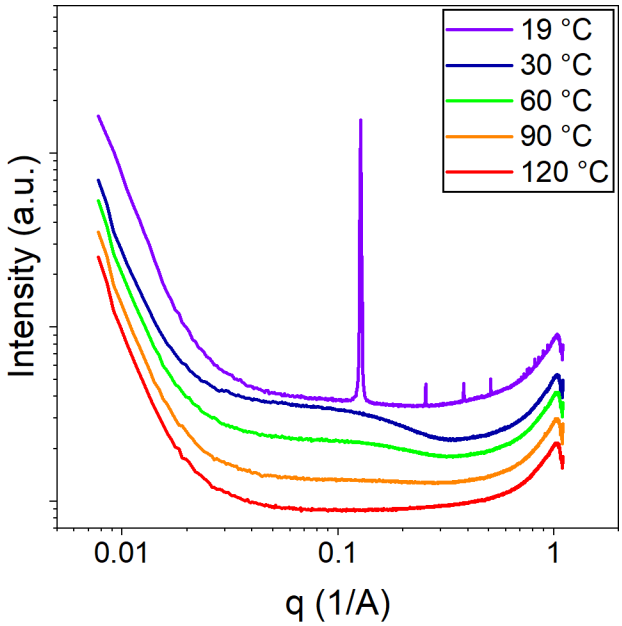

Figure 5.1: 1D linescans glycerol monooleate at various temperatures. The sample corresponds to a 5 wt% GMO in white oil.

The features at q > 0.4 Angstroms and the rise in background scattering may be attributed to the thermal diffuse scattering originating from the white oil solvent. Scattering from white oil only over the same temperature range is shown in Figure 2. Plots are not scaled to demonstrate the rise in intensity from background scattering with temperature.

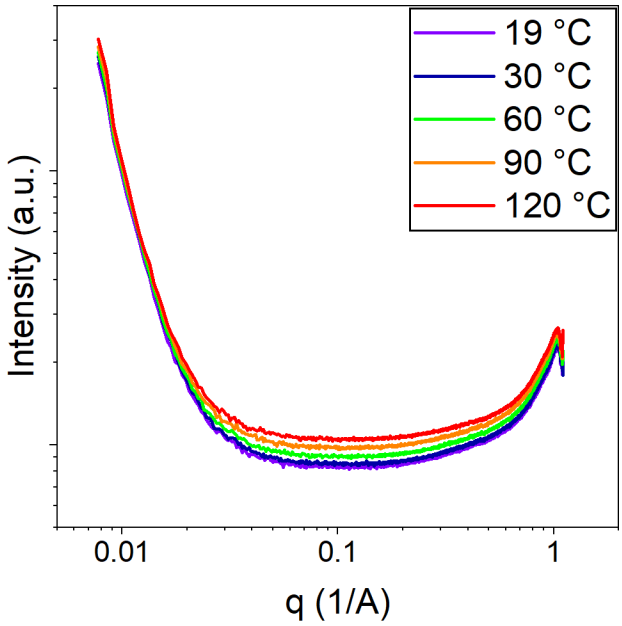

Figure 5.2: 1D linescans for pure white oil at various temperatures. Linescans are not shifted, demonstrating the rise in intensity with temperature due to thermal background scattering.

Sharp, diffraction-like scattering is designated ‘structure’ in the phase diagram presented in Figure 3, broad form factor scattering is designated ‘micelle’, and no features designated ‘disorder’. Observation of Figure 3a reveals that below ~1 wt% of GMO, structure factor peak dissolve directly into no features without an intermediate micelle phase. Above ~5 wt%, an intermediate micelle phase is observed. The temperature at which this micelle feature disappears rises steadily with monoglyceride concentration. These trends are duplicated in Figure 3b for GMS, with shifts in the transition temperature.

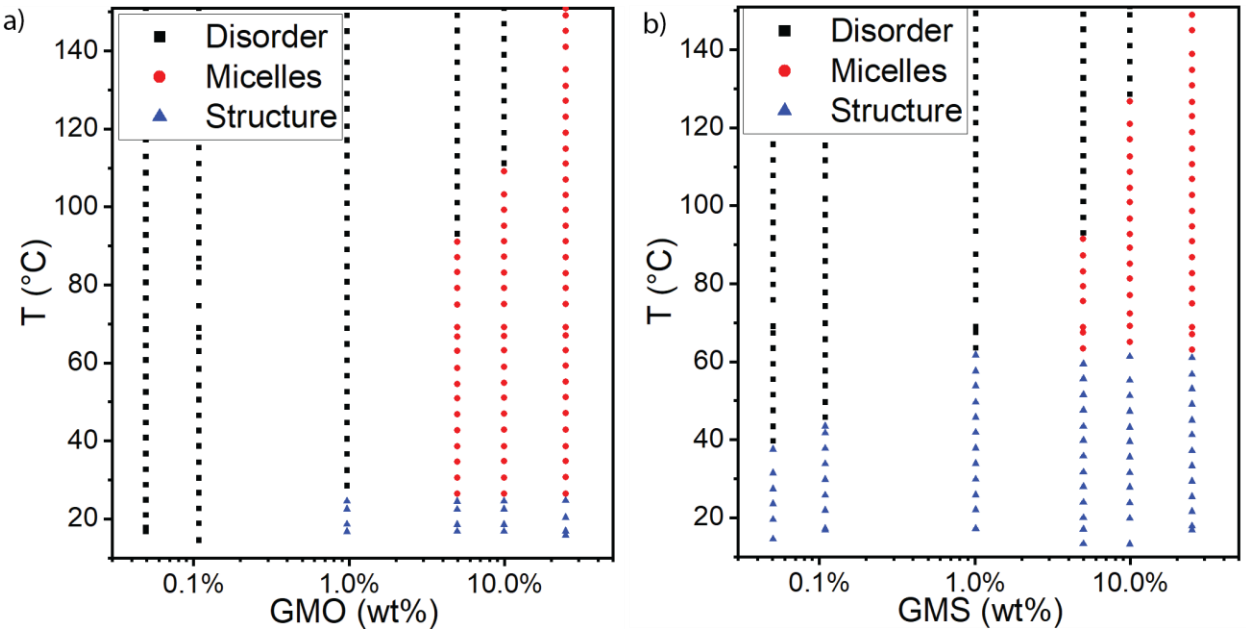

Figure 5.3: Phase diagrams of a) glycerol monooleate and b)glycerol monostearate. Two transitions are observed, from a crystalline phase ('Structure') to a micelle phase, and from a micelle phase to featureless background scattering ('Disorder').

It is worthwhile to note that there is some level of skepticism in the reverse micelle community that a true water-free reverse micelle can be formed. Even in the case of carefully dried materials, water can remain bound to the hydrophilic portions of a molecule [16]– thus, it is experimentally quite difficult to produce a completely dry system. A few claims have been made of water-free reverse micelle formation. [3] However, modeling and simulation work has indicated that truly water-free systems do not form micelles. Meanwhile, even exceedingly trace water can be sufficient to drive reverse micelle formation. [9,17] Thus, it is likely that the reported nominally "water-free" systems rely on the presence of trace water to drive micelle formation. In light of this, it is likely that our system similarly relies on trace water, even in the case where no additional water is added, to drive reverse micelle formation.

5.6 Effect of Water Addition

Following the observation of micelle formation above a threshold monoglyceride concentration, the effect of water addition was explored. The stated objective of this work was to identify potential micelle-forming formulations at conditions close to typical process conditions. Since biofeedstocks are typically blended at moderate fractions and heated to high temperatures, higher micelle dissolution temperatures were desired. It was hypothesized that the hydrogen bonding provided through additional water molecules would stabilize the micelles to higher temperatures. Phase diagrams for samples containing 5 wt% monoglyceride, at various water contents, are shown in Figure 4. The convention is followed from Figure 3 in assigning phases. Water contents were chosen in the approximate range of those typically observed from the autoclave experiments in the previous section.

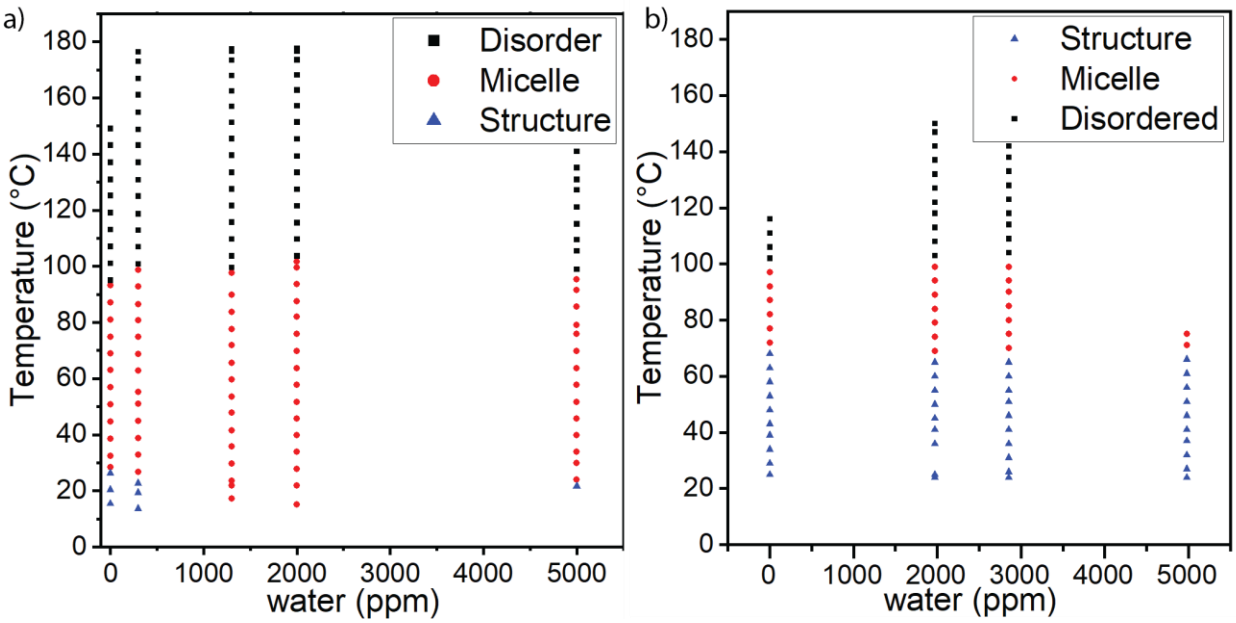

Figure 5.4: Phase diagrams of a) glycerol monooleate and b)glycerol monostearate at with various amounts of added water. The structure transition is seen to shift to lower temperature with added water, and the micelle transition rises slightly in temperature.

It is visually apparent that in the case of GMO, the crystalline phase transition lowers slightly. The micelle transition also rises in temperature, and then stabilizes around 100 °C. The

crystalline transition of GMS remains comparatively stable, but the micelle transition temperature rises by a few degrees between 0 and 3,000 ppm of water. (The sample at 5,000 ppm melted and moved out of the trajectory of the beam). These transitions may be understood in terms of water disrupting the typical monoglyceride organization processes. For the crystalline transition, water molecules disrupt the carbon tail packing of the glycerol monooleate and cause the crystalline phase to disappear. Glycerol monostearate has a completely saturated alkyl backbone, and thus its crystallization is less affected by the addition of water. In contrast, the additional hydrogen bonding provided by water provides additional enthalpic incentive for monoglyceride molecules to remain aggregated as the temperature is raised for both monoglycerides.

The effect of temperature on the micelles may be measured through a model fit of the SAXS data. Figure 5.5 shows background-subtracted example data from a 5 wt% GMO with 1,300 ppm water sample at various temperatures. The data was fit to the Guinier-Porod model, representing dilute form factor scattering from monodisperse objects. Deviation of the experimental data from the model at low q may originate from micellar aggregation.

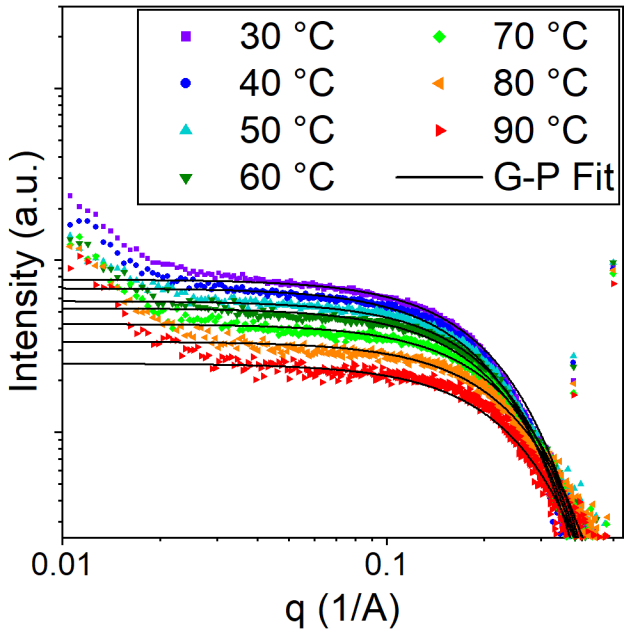

Figure 5.5: Background-subtracted 1D scattering for a 5 wt% GMO sample with 1,300 ppm water. Solid black line indicate a calculated fit of a Guinier-Porod model.

Data from the sample set at 10,000 ppm is shown in Figure 6. It is apparent that the slope leading into the first oscillation deviates from zero at low temperatures, indicating an elongation in the shape of the micelles. In both Figure 5 and Figure 6, it is apparent that the radius of gyration R_g changes with temperature.

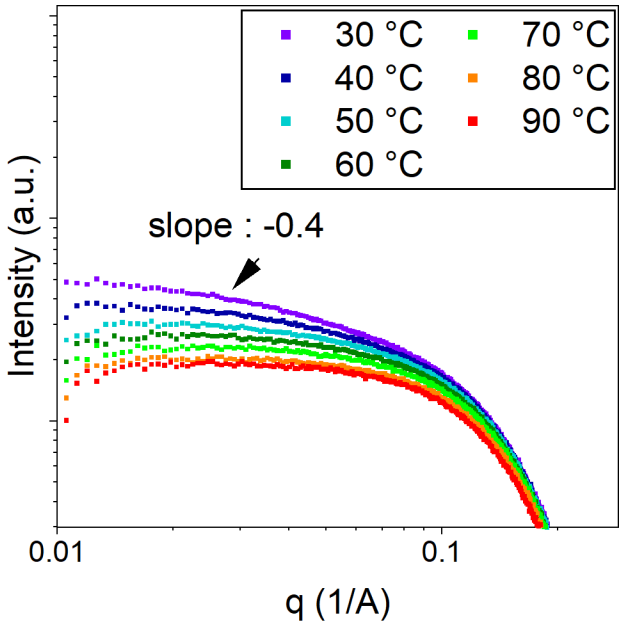

Figure 5.6: Background-subtracted 1-D scattering for a 5 wt% GMO sample with 10,000 ppm water. At cooler temperatures, the low-q slope deviates from zero, indicating elongation of the micelle.

The relationship between R_g, temperature, and water content is more apparent if the R_g is explicitly calculated from a model fit. The results from the Guinier-Porod model fit for a number of water-containing samples are shown in Figure 7a. It is apparent that the modeled R_g shrinks with higher temperature, which is consistent with our understanding of gradual micelle dissolution a higher temperature. Interestingly, R_g initially shrinks with added water, and then rises again. Corresponding aggregation numbers N_{agg} in Figure 7b were calculated by estimating the micelles as monodisperse geometric spherical objects. Although this is not a strictly correct assumption for the higher water content samples, the general trends are still informative. Knowing that R_g is related to the physical radius of a sphere, R, according to the equation:

$$R_g^2 = \frac{3*r^2}{5}$$

the aggregation number may be calculated with knowledge of the molar volume, v_m, which is the density divided by the molecular weight. In this case, since the carbon tails of a

monoglyceride are quite similar in electron density to the white oil, the electron contrast for scattering is likely only sufficient in the polar headgroup of the molecule. The molecular weight used is thus the molecule consisting of only the polar headgroup of the monoglyceride (1-monobutyrin, molecular weight of 162.18 g/mol).

$$N_{\text{agg}} = \frac{4*\pi*r^3}{3*v_m}$$

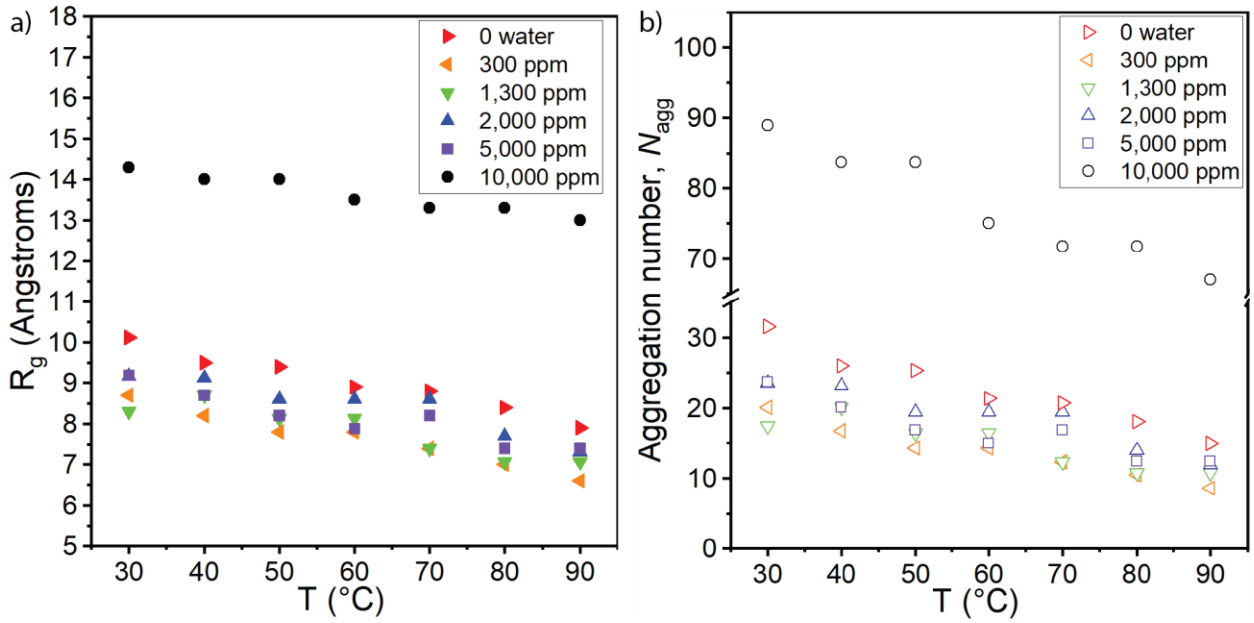

Figure 5.7: *a)* Calculated radius of gyration Rg for 5 wt% GMO samples with various amounts of water, calculated by a Guinier-Porod fit of the experimental data. *b)* Calculated aggregation number for the samples in part a), representing the average number of molecules within the micelle.

From these data, the amount of water present can be said to affect the micelle formation and geometry. When only a small amount of water is present, the micelles are slightly smaller. This can be understood as the water altering the entropic-enthalpic balance by providing additional hydrogen bonding in the micelle core. Thus, fewer monoglyceride molecules are required to overcome the entropy loss from aggregation. When the amount of water increases,

the core of the micelle is swollen by the additional water and is able to accommodate more monoglyceride molecules. Eventually, the micelle elongates to accommodate a large amount of additional water. At 10,000 ppm of water, there is 5 times as much monoglyceride by weight (at 5 wt%, or 50,000 ppm). Correcting for the difference in molecular weight, this is the equivalent of about 4 water molecules per monoglyceride molecule.

5.7 Effect of fatty acid

Since fatty acids are the primary breakdown product of triglycerides (and a major contributor to corrosion), it was important to determine the effect of fatty acid addition on the reverse micelles. The phase diagrams of a 5 wt% monoglyceride solution in white oil with no added water (Figure 5.8a) or 10,000 ppm water (Figure 5.8b) and varying amount of oleic acid added are shown in Figure 8a. It is apparent that the addition of fatty acid modifies the boundaries of the phase diagram significantly in both cases. In the case of no water, the transition between the crystalline and micellar phase gradually lowers in temperature and then disappears. Meanwhile, the micelle transition temperature lowers by ~20 °C in both cases. These data

suggest that fatty acid destabilizes the reverse micelles.

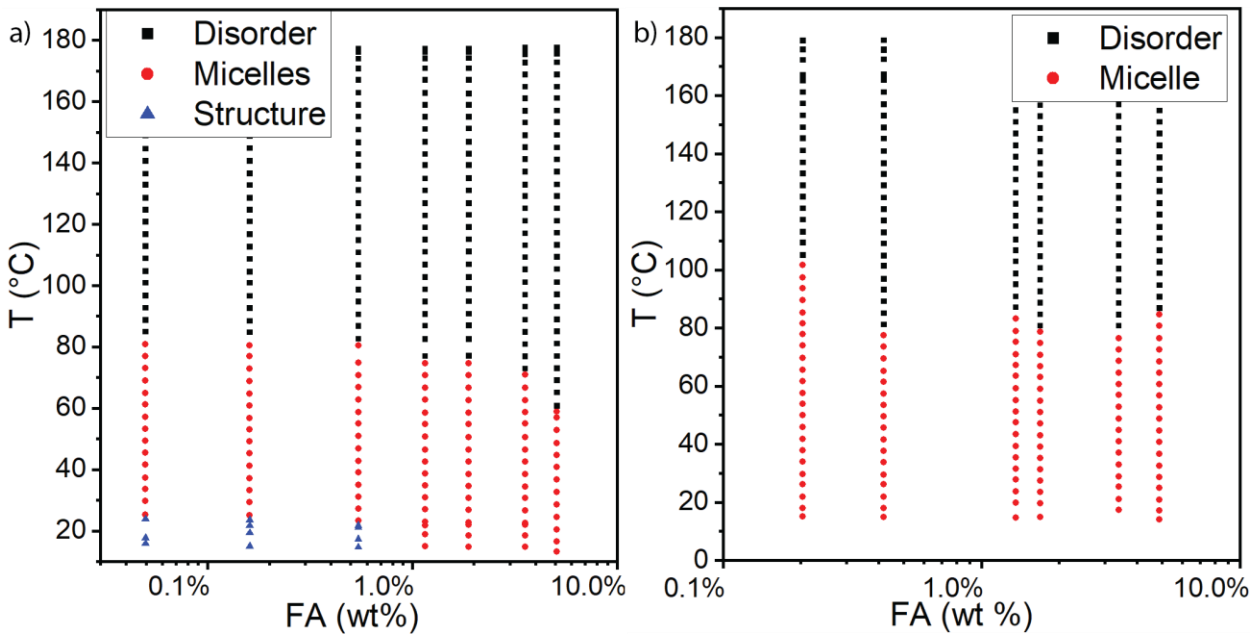

Figure 5.8: Phase diagram representing 5 wt% GMO sample with various amounts of fatty acid *a*) with no added water *b)* with 10,000 ppm added water.

In addition to the overall trends visible in the phase diagram, careful inspection of the 1-D linescans reveal additional trends worth examining. An example series of 1-D linescans are shown in Figure 9 for 5 wt % GMO, no water, and various amounts of fatty acid addition at 50 °C. Linescans are shifted vertically for clarity. Only subtle differences in R_g are observed up to ~1 wt% fatty acid. Greater fractions of fatty acid result in a qualitative change in the scattering, with the emergence of a peak maximum associated with structure factor scattering. These may be seen clearly as deviations from the Guinier-Porod model at higher fatty acid fractions.

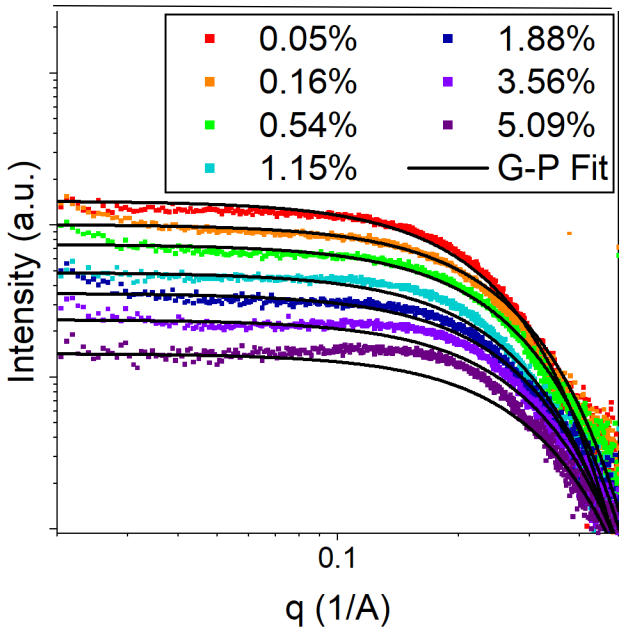

Figure 5.9: 1-D linescans of a 5 wt% GMO sample with no water and various amounts of fatty acid. Linescans are vertically shifted for clarity. The solid black line represents a calculated fit of a Guinier-Porod model. Experimental data begins to deviate significantly from the calculated model at fatty acid content >1 wt%.

The differences in R_g observed below ~1 wt% fatty acid may be compared across temperature. Figure 10 plots the observed Rg at 30 °C and 90 °C for various fatty acid fractions, both with water at 10,000 ppm and no water. No clear trend emerges, suggesting that in this composition range fatty acids have only minor effects on the size and geometry of the micelle.

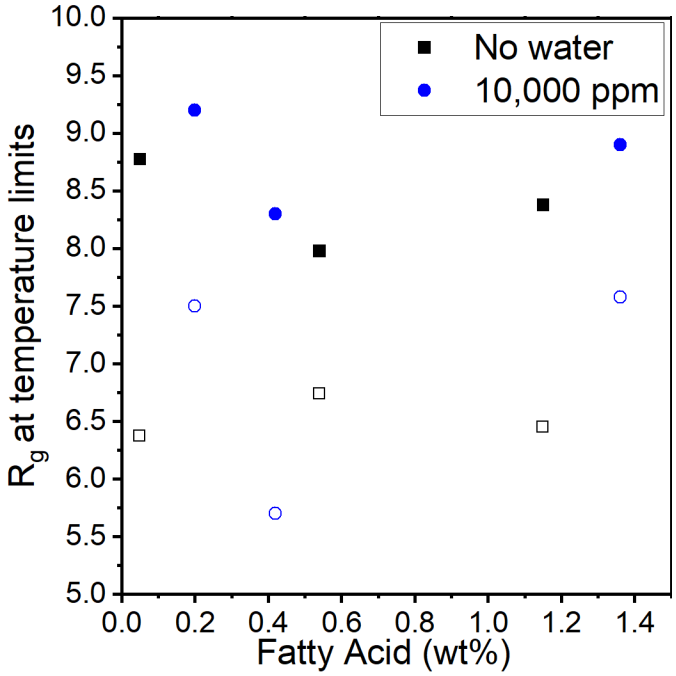

Figure 5.10: Calculated Rg from the Guinier-Porod model fits of 5 wt% GMO samples with either no water or 10,000 ppm of water at various amounts of fatty acid. Calculated Rg at two temperatures, 90 °C (open data) and 30 °C (filled data) are shown.

At higher fatty acid fractions, the emergence of a scattering maximum requires more careful consideration. In previous works, a similar peak [10,18] has appeared in reverse micelle samples. These peaks are attributed to intermicellar repulsion, with the origin in a combination of short-range attraction and long-range repulsion resulting in equilibrium clustering of objects. Interestingly, a similar peak appears in samples with elevated monoglyceride content (Figure 5.11), implying that the origin of the peak is fundamentally a concentration effect. As the concentration of amphiphile increases, the solution can no longer be considered dilute and intermicellar interactions appear in the form of structure factor scattering. The fact that structure factor interactions appear when adding fatty acid as well as additional monoglyceride suggests that at least some fatty acid is actually getting incorporated into the micelles. This is particularly promising for the hypothesis that polar species (e.g. fatty acids) will sequester into reverse micelles in nonpolar solutions, and thus be less corrosive to their environment.

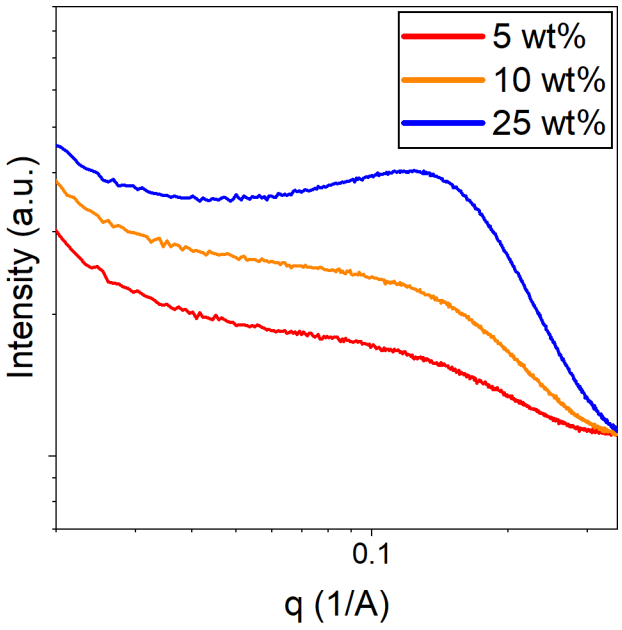

Figure 5.11: 1-D linescans of GMO in white oil at various concentrations. A clear intensity maximum appears, indicating structure factor scattering corresponding to a non-dilute solution. The peak appears in roughly the same location as in Figure 5.5.

5.8 Conclusions & Outlook

In this section, we have developed a number of phase diagrams elucidating the role of composition, temperature, and various additives on the size and stability of reverse micelles formed by monoglycerides in nonpolar long-chain alkyl oils. A critical concentration is observed, below which the crystalline monoglyceride directly dissolves in the oil with no intermediate micelle or aggregate phase. Above a critical concentration and below a critical temperature, an intermediate micelle phase is observed. Fitting of the SAXS data reveals that aggregate size shrinks steadily as temperature is increased, which is consistent with the understanding of increased solubility of the monoglyceride with increased temperature. The addition of water initially shrinks the average micelle size, but with additional water the micelle grows again and eventually transitions to a more elongated shape. In addition, the micelle

dissolution temperature rises slightly with added water. In contrast, the addition of fatty acid lowers the micelle dissolution temperature. The addition of fatty acid above ~1 wt% results in a qualitative change in the x-ray scattering, with the emergence of an intensity maximum consistent with structure factor scattering. Sufficiently concentrated monoglyceride solutions with no water or fatty acid demonstrate an intensity maximum at approximately the same length scale, implying that adding fatty acid concentrates the micelle solution in the same fashion as additional monoglyceride. This suggest that fatty acids are actually incorporated into the reverse micelle as co-surfactants, rather than dissolving into the oil.

The conclusions from this work lay the foundation for the future design of low-corrosion biofeedstocks. Although the micelle features of low-concentration monoglyceride solutions dissolved well below working temperature of 275 °C in the previous section, the general trends demonstrate that there is significant opportunity to design micelle solutions stable to high temperatures. For instance, incorporating small amounts of surfactants with a larger polar headgroup (e.g. lecithin) may alter the phase boundaries in the same way as increasing the amount of monoglyceride. Small amounts of such surfactants are expected to be present in biofeedstocks as residues of the purification process. In addition, our work has demonstrated that the presence of a polar solvent alters the micellization behavior of the monoglyceride. Future work may explore the effect of different polar solvents on reverse micelle stability and geometry. In addition, our work suggests that fatty acids free become incorporated into the reverse micelle, but it is unclear if there is an upper incorporation limit to the fatty acid, or intermediate phase transitions within the range of fatty acid solubility. In addition, the key question of whether a reverse-micelle forming solution is actually less corrosive than a homogeneous solution is

unanswered. Future work may focus on experiments that extend this groundwork into the design of practical biofeedstock formulations.

References

1. Ruckenstein, E., Nagarajan R. Aggregation of Amphiphiles in Nonaqueous Media. *J Phys Chem*. 1980;84:1349-1358.
2. Verbeeck A, Voortmans G, Jackets C, Schryver FC De. Characterization and Stabilization of Inverse Micelles. 1989;3(1):766-776.
3. Correa NM, Silber JJ, Riter RE, Levinger NE. Nonaqueous polar solvents in reverse micelle systems. *Chem Rev*. 2012;112(8):4569-4602. doi:10.1021/cr200254q
4. Mukerjee P, Mysels KJ. Critical Micelle Concentrations of Aqueous Surfactant systems. *United States Dep Commer Natl Bur Stand*. 1971;(NSRDS-NBS 36).
5. Smith GN, Brown P, Rogers SE, Eastoe J. Evidence for a critical micelle concentration of surfactants in hydrocarbon solvents. *Langmuir*. 2013;29(10):3252-3258. doi:10.1021/la400117s
6. Falcone RD, Correa NM, Silber JJ. On the formation of new reverse micelles: A comparative study of benzene/surfactants/ionic liquids systems using uv-visible absorption spectroscopy and dynamic light scattering. *Langmuir*. 2009;25(18):10426-10429. doi:10.1021/la901498e
7. Matter S, Shrestha LK, Shrestha G, De KA. Reverse micelle microstructural transformations induced by oil and water. 2011:10017-10024. doi:10.1039/c1sm06047c
8. Bradley-Shaw JL, Camp PJ, Dowding PJ, Lewtas K. Self-assembly and friction of glycerol monooleate and its hydrolysis products in bulk and confined non-aqueous

solvents. *Phys Chem Chem Phys*. 2018;20(26):17648-17657. doi:10.1039/c8cp01785a

9. Bradley-Shaw JL, Camp PJ, Dowding PJ, Lewtas K. Glycerol monooleate reverse micelles in nonpolar solvents: Computer simulations and small-angle neutron scattering. *J Phys Chem B*. 2015;119(11):4321-4331. doi:10.1021/acs.jpcb.5b00213
10. Shrestha LK, Shrestha RG, Aramaki K. Intrinsic parameters for the structure control of nonionic reverse micelles in styrene: SAXS and rheometry studies. *Langmuir*. 2011;27(10):5862-5873. doi:10.1021/la200663v
11. Shrestha LK, Shrestha RG, Varade D, Aramaki K. Tunable parameters for the structural control of reverse micelles in glycerol monoisostearate/oil systems: A SAXS study. *Langmuir*. 2009;25(8):4435-4442. doi:10.1021/la8039225
12. Klíčová L, Šebej P, Štacko P, et al. CTAB/water/Chloroform reverse micelles: A closed or open association model? *Langmuir*. 2012;28(43):15185-15192. doi:10.1021/la303245e
13. Shrestha LK, Dulle M, Glatter O, Aramaki K. Structure of polyglycerol oleic acid ester nonionic surfactant reverse micelles in decane: Growth control by headgroup size. *Langmuir*. 2010;26(10):7015-7024. doi:10.1021/la904231t
14. Ilavsky J, Jemian PR. Irena: Tool suite for modeling and analysis of small-angle scattering. *J Appl Crystallogr*. 2009;42(2):347-353. doi:10.1107/S0021889809002222
15. Pitzalis P, Monduzzi M, Krog N, Larsson H, Ljusberg-Wahren H, Nylander T. Characterization of the liquid-crystalline phases in the glycerol monooleate/diglycerol monooleate/water system. *Langmuir*. 2000;16(15):6358-6365. doi:10.1021/la0002031
16. Eriksson PO, Lindblom G. Lipid and water diffusion in bicontinuous cubic phases measured by NMR. *Biophys J*. 1993;64(1):129-136. doi:10.1016/S0006-3495(93)81347-X
17. Vierros S, Österberg M, Sammalkorpi M. Aggregation response of triglyceride hydrolysis

products in cyclohexane and triolein. *Phys Chem Chem Phys*. 2018;20(42):27192-27204. doi:10.1039/c8cp05104f

18. Penttilä PA, Vierros S, Utriainen K, et al. Phospholipid-Based Reverse Micelle Structures in Vegetable Oil Modified by Water Content, Free Fatty Acid, and Temperature. *Langmuir*. 2019. doi:10.1021/acs.langmuir.9b01135

CHAPTER 6: CONCLUSION

In this work, we have presented two different systems of self-assembled amphiphile phase evolution under elevated temperatures. Using a combination of x-ray scattering and techniques common to soft materials characterization, we have identified details of the phase behavior and factors that lead to phase transitions.

In the first system, we showed that ionic liquids are effective phase modifiers for block copolymers in epoxy solutions. Lyotropic phases with multiple structure factor peaks in SAXS (corresponding to long-range order) are observed by simply blending together block copolymer, epoxy, and ionic liquid. The classic diblock phases were observed at a variety of concentrations in a full ternary phase diagram. In a different polymer system, structure factor scattering and form factor scattering were both observed in low-concentration solutions of PEP-PEO and PI-PEO with ionic liquid and epoxy. Upon curing, the complex phase behavior exhibited by the ternary blends of block copolymer, ionic liquid, and epoxy evolve significantly when the epoxy is cured. The complexity of these phase changes offers possibilities in engineering materials with a wide variety of possible nanostructures controlled via cure cycle.

In the second system, a blend of acylglycerols and long-chain alkyl oils was subjected to thermal breakdown by a high-temperature hold for extended periods of time. The acylglycerol molecules were found to break down readily under these conditions, generating a variety of relatively more polar thermal breakdown products. A variety of reverse-micelle forming solutions were fabricated from species expected to be generated during this breakdown process. The approximate size and shape of these micelles was identified, as well as their dissolution temperature.

Although the types of molecules in these two systems are quite different, in both cases the governing free energy landscape led to spontaneous self-assembly of amphiphiles in their environment. This behavior is foundational to a number of subfields in soft materials and has been studied by generations of scientists. However, it continues to offer new and surprising avenues of scientific inquiry. The interplay of thermodynamic and kinetic factors that govern real-world systems offers sufficient complexity for any number of detailed studies, and new theoretical insights are always emerging. In this work, we have attempted to rationalize our observations from our theoretical understanding of the factors that affect self-assembly. These efforts expand our understanding of self-assembly in complex systems and the relevant parameters required to fabricate self-assembled materials.